A HIGH STATISTICS STUDY OF LAMBDA BETA DECAY

by
Jay Samuel Dworkin

A dissertation submitted in partial fulfillment
of the requirements for the degree of
Doctor of Philosophy
(Physics)
in The University of Michigan
1983

Doctoral Committee:

Professor Oliver E. Overseth, Chairman
Associate Professor Martin B. Einhorn
Professor Robert R. Lewis
Associate Professor Richard L. Sears
Associate Professor Rudolf P. Thun

AMB1798

ABSTRACT

A HIGH STATISTICS STUDY OF LAMBDA BETA DECAY

by

Jay Samuel Dworkin

Chairman : Oliver E. Overseth

A sample of 55,752 lambda beta decays has been detected in the Fermilab Neutral Hyperon Beam. A synchrotron radiation detector and a lead glass array together provided a rejection factor in excess of 10^4 against the non-leptonic lambda decay mode. The ratio of the axial vector to vector coupling constants in lambda beta decay has been determined. The values obtained are -0.757 ± 0.019 and $+0.777 \pm 0.019$, where the errors are purely statistical. The systematic uncertainty presently assigned to each of these values is ± 0.080; work is in progress to improve their accuracy.

The branching ratio for lambda beta decay has also been measured. The result is $(8.15 \pm 0.69) \times 10^{-4}$, where the systematic uncertainty has been included in the error.

ACKNOWLEDGEMENTS

I am very grateful to Oliver Overseth for his continued support, encouragement and patience during the course of my graduate study. I would also like to thank the rest of my collaborators; my association with the Neutral Hyperon Group at Fermilab has been extremely rewarding. I am particularly indebted to Ken Heller and Bob Handler for contributing invaluable help and advice throughout the duration of this project. The leadership and insight provided by Lee Pondrom were essential to the success of this experiment. Andy Beretvas, Tim Cox, Tom Devlin, Kam-Biu Luk and Marleigh Sheaff deserve a special note of thanks for their helpful suggestions. It is a pleasure to acknowledge the contributions of George Ott, Jesse Jaske, and Erhardt Behr, who provided superb technical support. I would also like to thank Augusto Garcia for many helpful conversations.

This experiment would not have been possible without the cooperation and support of the staff at Fermilab.

TABLE OF CONTENTS

LIST OF FIGURES

LIST OF TABLES

CHAPTER 1

INTRODUCTION

Hyperon semi-leptonic decays provide a sensitive test of weak interaction models. However, the accumulated experimental data for such processes have been limited by statistics. The advent of secondary hyperon beams at high energy particle accelerator laboratories, containing high fluxes of the short-lived strange particles, is an important step towards overcoming this obstacle. The detection of a rare semi-leptonic decay in such a hyperon beam, suppressed by a factor of 10^3 relative to the more numerous non-leptonic decays, is the challenge addressed in this thesis.

The results from an experiment designed to accumulate a large number of lambda beta decays are presented here.

The experiment was performed in the Fermilab Neutral Hyperon Beam by the Michigan, Minnesota, Rutgers, Wisconsin collaboration. A synchrotron radiation detector and a lead glass array were employed in the experiment to obtain a rejection factor in excess of 10^4 against the non-leptonic lambda decay mode. The final data sample, comprising 55,752 events, is more than a factor of four larger than the total published world data sample of lambda beta decays.

The formalism for hyperon beta decays is discussed in many textbooks [1]. The matrix element for the decay $\Lambda \to p e^- \bar{\nu}_e$ is the product of contributions from the matrix elements of the lepton current and the hadronic weak current:

$$\mathcal{M} = \frac{G}{\sqrt{2}} \langle p | V-A | \Lambda \rangle \bar{u}(l) \gamma_\mu (1-\gamma_5) v(k) ,$$

where G is the universal weak coupling constant, with the value 1.16×10^{-5} GeV^{-2}. The electron momentum four-vector in the center-of-mass (c.m.) frame is denoted by $l_\lambda = (e, \vec{l})$. The anti-neutrino, subsequently referred to as the neutrino for convenience, has the c.m. momentum four-vector $k_\lambda = (\nu, \nu \hat{k})$.

The hadronic weak current can be written according to the conventions of the Particle Data Group [2]:

$$\langle p|V-A|\Lambda\rangle = \bar{u}(P')\left[\gamma_\mu(g_V - g_A\gamma_5) + \frac{g_W}{M_\Lambda} i\sigma_{\mu\lambda}q^\lambda\right]u(P).$$

The four-momentum transferred to the leptons in the c.m. frame is $q_\lambda = P_\lambda - P'_\lambda = \ell_\lambda + k_\lambda$; P_λ and P'_λ are the four-momenta of the lambda and the proton. The coefficients g_A , g_V and g_W are, respectively, the axial vector, vector and weak magnetism coupling constants for lambda beta decay. The same formalism applies to the other hyperon semi-leptonic decays; there are a set of coupling constants with different values for each process.

The differential decay rate for lambda beta decay can be found according to:

$$d\Gamma = \frac{1}{(2\pi)^5}\delta^4(P' + \ell + k - P)\,|\mathcal{M}|^2 M_p M_e \frac{d^3P'}{E_p}\frac{d^3\ell}{e}\frac{d^3k}{2\nu}.$$

The result for unpolarized lambda hyperons has been

calculated by Garcia [3] and is presented here:

$$d\Gamma = \frac{G^2}{(2\pi)^5} \frac{\beta e^2 \nu^3}{e_m - e} \left(D_1 + x\beta D_2 \right) de\, d\Omega_e\, d\Omega_\nu ,$$

where

$e_m = \frac{M_\Lambda^2 - M_p^2}{2 M_\Lambda}$ = 163.244 MeV is the maximum value of the c.m. electron energy,

$\beta = |\vec{p}|/e$ is the c.m. electron velocity,

$x = \hat{\ell} \cdot \hat{k} \equiv \cos\theta_{e\nu}$ is the cosine of the angle between the electron and neutrino directions in the lambda rest frame,

$\nu = \frac{e_m - e}{1 - \frac{e}{M_\Lambda}(1 - \beta x)}$ is the c.m. neutrino energy,

and D_1 and D_2 are both linear functions of the kinematic variables e and x, as well as quadratic functions of the coupling constants. These functions will be described in detail in Chapter 5.

This expression can be integrated over angles and energy to obtain the decay rate as a function of the

coupling constants. Expanded to first order in the parameter δ, the result is [4]:

$$\Gamma = G^2 \frac{(\Delta m)^5}{60\pi^3} (g_V^2 + 3g_A^2)(1 - \tfrac{3}{2}\delta),$$

where $\delta = \frac{\Delta m}{M_\Lambda} = \frac{M_\Lambda - M_p}{M_\Lambda} = 0.16$. This can be converted into an expression for the experimentally accessible branching ratio with an additional multiplicative factor of 2.623×10^{-10} sec, the measured value of the lambda mean lifetime [2].

The electron-neutrino correlation (α_{ev}) is sensitive to the magnitude of the ratio of the axial vector to vector coupling constants (g_A/g_V), and can be calculated to first order in the parameter δ [4]:

$$\alpha_{ev} \equiv 2 \frac{\Gamma(0 < x \leq 1) - \Gamma(-1 \leq x < 0)}{\Gamma(-1 \leq x \leq 1)} = \frac{g_V^2 - g_A^2}{g_V^2 + 3g_A^2} - \delta.$$

The magnitude of g_A/g_V was extracted from the experimental data by measuring the angular distribution of the neutrino relative to the electron direction in the rest frame of the decaying lambda hyperons.

The Cabibbo theory [5], discussed in Chapter 6, makes specific predictions concerning the values of the branching ratio and the ratio of the axial vector to vector coupling constants in lambda beta decay. The limited experimental results available show general agreement with this model, although more precise results are needed in order to probe the limits of its accuracy [6]. The world average values for these quantities are presently $(8.35 \pm 0.15) \times 10^{-4}$ for the branching ratio and -0.690 ± 0.034 for g_A/g_V [2]. The errors in these quantities are dominated by the contribution from a single recent experiment which accumulated 10,000 events, a sample more than a factor of five larger than the previously published world sample.

The determination of both the branching ratio and the ratio of the axial vector to vector coupling constants from the 55,752 lambda beta decays in this experiment is discussed in Chapter 5. The results are compared with the results from other experiments, as well as with theoretical predictions, in Chapter 6.

CHAPTER 2

EXPERIMENTAL TECHNIQUE AND APPARATUS

2.1 Design Considerations

This experiment was performed in the Fermilab Neutral Hyperon Beam. The detailed construction and operational characteristics of the neutral beam are described elsewhere [7]. Its salient features are reviewed in Section 2.2. The beam contained neutral strange particles, suppressed by a factor of 10^2 relative to a higher flux of neutrons and photons. Lambda hyperons were detected by observing their charged decay products in a magnetic spectrometer assembled behind the decay region. A lambda beta decay ($\Lambda \rightarrow p e^- \bar{\nu}_e$) had the same signature in the magnetic spectrometer as a non-leptonic lambda decay

($\Lambda \rightarrow p\pi^-$). This signature, referred to as a neutral vee topology, consisted of two oppositely charged particles emanating from a single point in the decay region. The information from the spectrometer that allowed the neutral vee events to be studied offline was retrieved and stored by the data acquisition system described in Chapter 3. This process was initiated by an electronic trigger. The purpose of a trigger in a high rate high energy physics experiment is to examine prompt pulses from various detector elements in order to decide if a group of logical requirements has been met. These requirements are designed to ensure the efficient selection of the desired events. A discussion of the trigger employed to select the neutral vee events is also contained in Chapter 3.

Lambda beta decay is a rare process which is suppressed by a factor of 10^3 relative to non-leptonic lambda decay. Thus it was crucial to supplement the magnetic spectrometer with electron detectors in order to discriminate between an electron from a lambda beta decay and the flood of negatively charged pions from non-leptonic lambda decays. Two methods of electron identification were employed in this experiment. The principles behind the operation of the synchrotron radiation detector and the lead glass electromagnetic shower detector are described later in this chapter. Both devices contributed to the

trigger selecting the lambda beta decays. These contributions will be discussed in Chapter 3. The event information from both detectors was then used offline to provide the hadronic rejection necessary to identify a clean sample of lambda beta decays; this is discussed in Chapter 4.

Another consideration was that other rare processes suppressed by factors of 10^2 relative to non-leptonic lambda decay could compete with the lambda beta decays if they had the neutral vee topology and satisfied the requirements of the electron detectors. The semi-leptonic decay of the long-lived K^o_L meson ($K^o_L \rightarrow \pi^+ e^- \bar{\nu}_e$), denoted Ke3, provides an example of such a process. Another was pair production by the photons from the neutral beam in the small amount of material in the decay region. These were handled by employing a threshold Cerenkov counter to distinguish protons, required in lambda beta decays, from the higher velocity positrons and positively charged pions in the undesired background. The threshold Cerenkov counter is described in Section 2.6. The usefulness of the counter in the trigger is discussed in Chapter 3.

Finally, an attempt was made to minimize the amount of material in the path of the neutral beam. This served to reduce the charged particle flux through the spectrometer

which resulted from neutral beam interactions. The multi-wire proportional chambers used in the magnetic spectrometer could thus operate with a reasonable efficiency in the beam region. It also helped to prevent any degradation of the momentum resolution of the magnetic spectrometer arising from either multiple Coulomb scattering of the detected charged particles, or from bremsstrahlung by an electron in a semi-leptonic decay.

2.2 The Production and Detection of Neutral Hyperons

Figures 1 and 2 show the plan and elevation views of the apparatus used for this experiment. The 400 GeV/c diffracted proton beam in the Fermilab M-2 beamline was directed onto a fixed beryllium target. The intensity of the incident proton beam was monitored by the argon-filled ionization chamber IC. The position and size of the proton beam were monitored by the SWIC, a segmented wire ion chamber which provided a beam profile in both the horizontal and vertical views. Normally 80% of the proton beam was contained within the area of the 3 mm diameter cylindrical production target.

The resulting proton-nucleon collisions gave rise to secondary hadrons which were used to form the neutral beam.

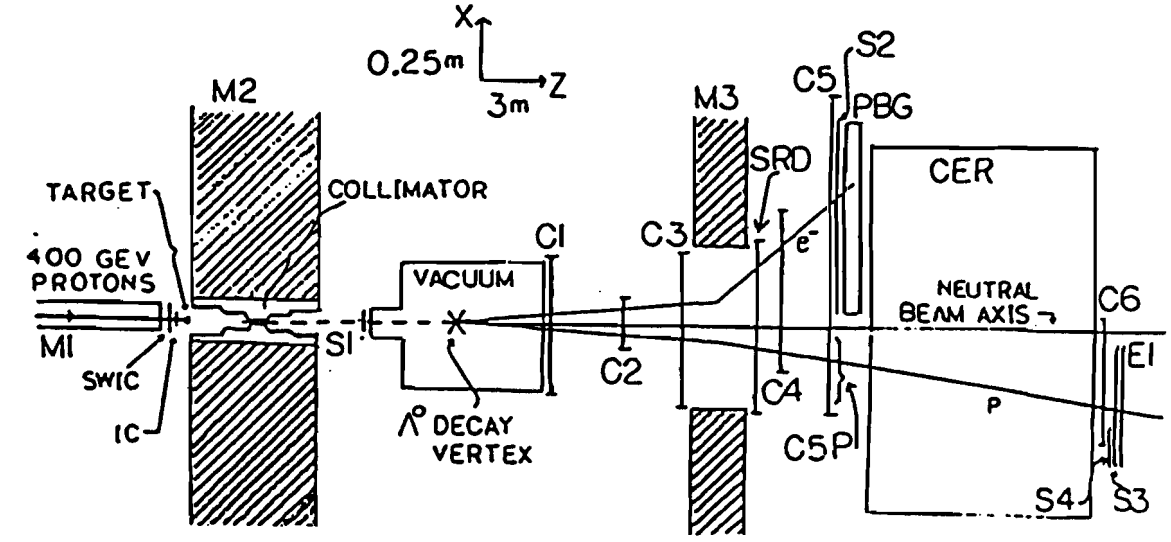

Figure 1. Apparatus - Plan View

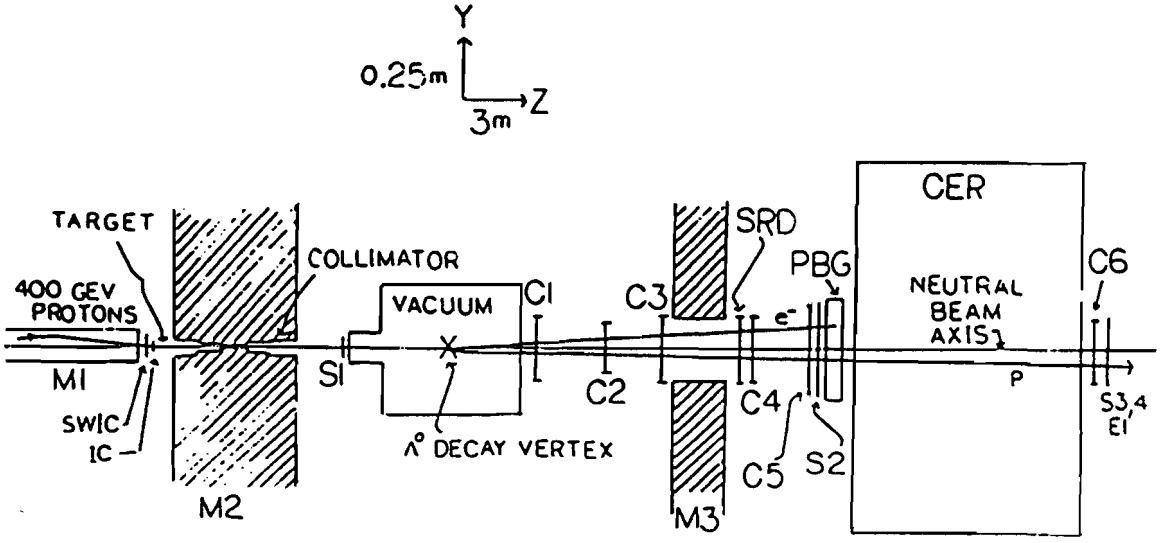

Figure 2. Apparatus - Elevation View

The 1/2 interaction length production target was aligned before the upstream aperture of a collimation system [8], which included a 4 mm diameter defining hole near the center of a 5.3 m long brass channel imbedded in the 23 kG vertical magnetic field of the M2 magnet. This magnetic field deflected both the proton beam and charged secondaries out of the neutral beam, which emerged from the 11 mm diameter exit aperture of the collimator. The outgoing neutral beam direction defined by the collimator axis ($+\hat{z}$), the vertical magnetic field in the collimator ($+\hat{y}$ upwards) and the horizontal $\hat{x}$ direction formed a right-handed orthogonal coordinate system which was used to describe the location of the elements comprising the apparatus. The dipole magnet M1, located upstream of the production target, was used to vary the angle between the incident proton direction and the outgoing neutral beam direction. As illustrated in Figure 2, the incident proton beam was first deflected a few centimeters vertically and then restored to the production target. This experiment accumulated equal amounts of data at two such production angles, +7.6 milliradians and -7.6 milliradians.

A 10 cm diameter scintillation counter, denoted S1, was placed 1.9 m downstream of the collimator exit aperature. This counter was used to veto charged particles and defined the beginning of the decay region 7.3 m

downstream of the production target. The neutral strange particles detected decayed in an 11 m long, 35 cm diameter evacuated pipe following this counter. The neutral beam was about 2 cm in diameter with 1 milliradian total divergence in the decay region.

The charged decay products were detected downstream of the decay region in a magnetic spectrometer that included two sets of three multi-wire proportional chambers, denoted C1-C6 in Figures 1 and 2, which measured the x and y track coordinates upstream and downstream of the analyzing magnet M3. The homogeneous vertical magnetic field of M3 deflected negatively charged particles in the $+\hat{x}$ direction. The measured field integral corresponded to a transverse momentum kick ($P_\perp$) of 0.94 GeV/c. The coordinate information allowed a calculation of the bend angle α for a given track; the charged particle's momentum was then calculated from the equation $P = P_\perp / \alpha$.

The momentum measurement of the charged decay products in an event with the neutral vee topology allowed a calculation of the mass and the momentum of the neutral parent according to

$$M_o^2 = m_+^2 + m_-^2 + 2E_+E_- - 2\vec{P}_+ \cdot \vec{P}_-$$

$$\vec{P}_o = \vec{P}_+ + \vec{P}_- .$$

The mass combinations (m_+, m_-) were varied to identify $\Lambda \to p\pi^-$, $K^o_S \to \pi^+\pi^-$ and $\bar{\Lambda} \to \bar{p}\pi^+$ in the sample of detected neutral vees. The majority of the events detected with the neutral vee trigger were non-leptonic lambda decays; this is discussed in detail in Chapter 4.

2.3 The Magnetic Spectrometer

2.3.1 Analyzing Magnet (M3)

The superconducting dipole magnet used in the magnetic spectrometer had a 60 cm (horizontal) x 20 cm (vertical) aperture, an effective length of 190 cm and a peak central field of 18 kG. The entrance aperture of the magnet was located 19 m from the collimator exit. The final value of the field integral used in a charged particle's momentum measurement was determined precisely by comparing the measured K^o_S mass with its known value.

2.3.2 Multi-Wire Proportional Chambers (MWPC's)

Each of the MWPC's C1-C6 was of conventional

construction [9]. They all contained two perpendicular planes of parallel sense (anode) wires. All but C2 had vertical and horizontal planes. This chamber was rotated at 45° relative to the others to facilitate ambiguity resolution in the two track pattern recognition. There were a total of 2864 sense wires in the twelve sense planes used in the magnetic spectrometer. The number of sense wires per plane varied from 128(C1y) to 640(C5x) and the wire spacing was 2 mm. Planes of vertical cathode wires, typically held at a potential of -4200 volts, were placed 4.8 mm away on both sides of the sense planes. The gas ionized by the detected charged particles was a mixture of 85% argon, 15% isobutane and 0.2% freon which had been bubbled through liquid methalyl at 0° C.

Every sense wire was connected to an amplifier circuit which generated both a prompt and a delayed pulse when the detected anode signal exceeded a threshold of 1.2 mv. The prompt pulses were grouped together in OR circuits which were wired to represent hodoscope elements from each chamber. These hodoscope signals were sent to threshold discriminators which provided output pulses that could be used in the the trigger logic. When the trigger logic was satisfied, a pulse was sent back to the chamber electronics to store the identity of the active sense wires. This 100 ns wide pulse, denoted ST, was timed to arrive back at

the amplifier cards in coincidence with the internally delayed pulse originally generated by each active amplifier channel. The consequence of such a coincidence was to set a latch for each such channel. The address of the active wire corresponding to the latch was encoded by the hardware connected to the chamber; it was eventually retrieved by the data acquisition system.

2.3.3 Material in the Path of the Neutral Beam

Helium-filled polyethelene bags were placed in the regions between the chambers to minimize the amount of material in the path of the neutral beam. Typical single counting rates in the chambers were kept below 0.6 Mhz; the charged particle efficiency of the sense planes varied from 95-99%. The material located between the vacuum in the decay region and the analyzing magnet corresponded to 2% of a radiation length, with the 508 μm thick aluminum window on the downstream end of the decay pipe contributing almost 30% of the total. A 127 μm thick mylar window on the upstream end of the decay pipe was preceded by the 70 mm thick S1 scintillator and air. The region between the analyzing magnet and the Cerenkov counter contained 1.5% of a radiation length.

2.4 The Synchrotron Radiation Detector

The synchrotron radiation detector, denoted SRD in Figures 1 and 2 , was located immediately downstream of the analyzing magnet M3. The detector consisted of a multi-wire proportional chamber filled with xenon gas, amplification electronics, and a device referred to as the Xenon Data Processor. The Processor was mounted on the air conditioned aluminum box containing the chamber, and was used in the trigger selecting lambda beta decays. The purpose of the detector was to identify electrons, which emitted synchrotron radiation as they were deflected in the magnetic field of M3. Photoelectrons ejected from xenon atoms by the incident synchrotron radiation, in this case x-ray photons, were detected in the xenon chamber.

2.4.1 Synchrotron Radiation and Photoelectric Absorption

The total energy I radiated per meter by a relativistic electron in a magnetic field B(kG) is

$$I = (3.38 \times 10^{-9}) \gamma^2 B^2 \quad [\text{KeV/m}] .$$

The dimensionless synchrotron spectrum F(z) for a single

electron, where $z=\omega/\omega_c$ can be calculated and is shown in Figure 3. The critical frequency is defined by

$$\omega_c=(2.5\times10^{10})\,\gamma^2 B\ .$$

The majority of photons are emitted with an energy less than $E_c=\hbar\omega_c$. The number of photons emitted per unit path length is independent of the energy of the electron, depending only on the magnetic field strength. Assuming the average photon energy is equal to half the critical energy, the number of photons emitted per unit path length can be estimated to be $I/0.5E_c$. A useful review of the synchrotron radiation process is provided by Tucker [10].

A 10 GeV electron ($\gamma=2\times10^4$), typical of the electrons from lambda beta decays reaching the synchrotron radiation detector, radiated about 800 KeV while traversing the field region in M3. This energy was divided amongst approximately 14 photons, each with an energy below the critical energy of 114 KeV. These x-ray photons were emitted in the plane of the electron orbit in a narrow cone of half angle $\Theta=1/\gamma$ about the electron direction. A higher energy electron radiated the same number of photons with a higher average photon energy.

The total energy radiated by a charged pion is a

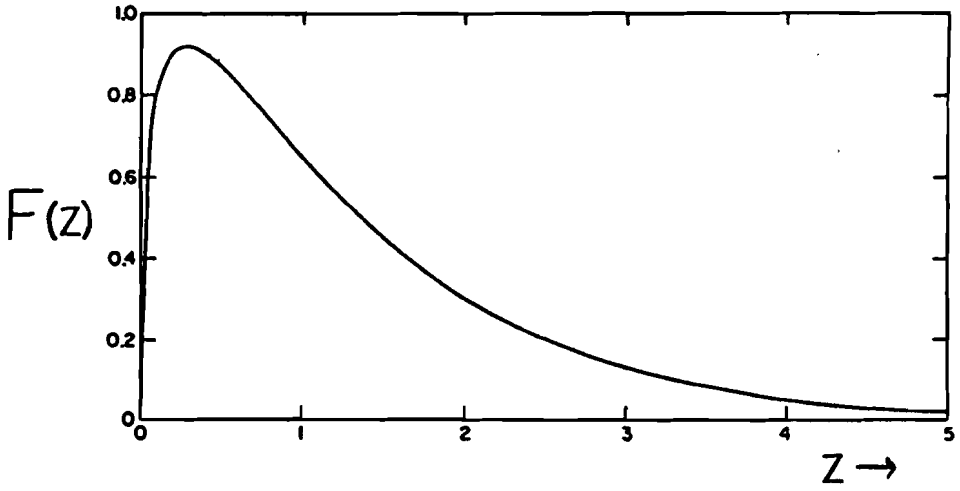

Figure 3. Dimensionless Synchrotron Radiation Spectrum F(z)

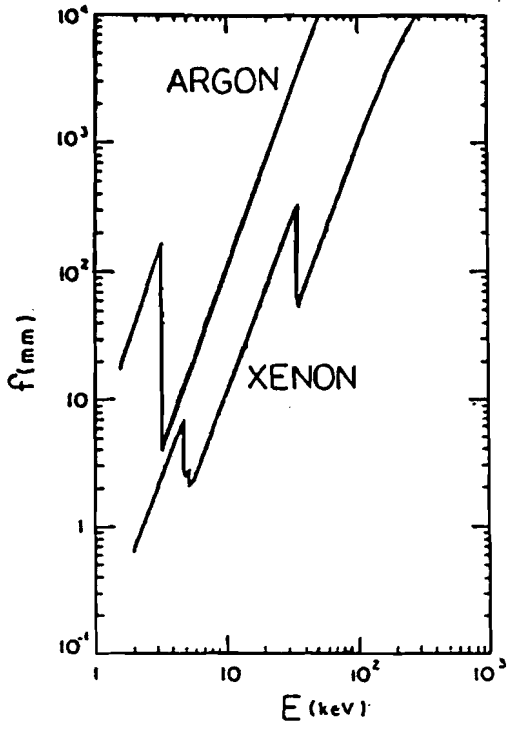

Figure 4. Absorption Mean Free Path for Photons

factor of $(m_e/m_\pi)^4 \sim 10^{-10}$ less than the energy radiated by an electron of the same momentum. The synchrotron radiation from the pions detected in this experiment was thus negligible, as the pion momentum spectrum for the detected non-leptonic lambda decays was similar to the electron spectrum from the lambda beta decays.

The absorption probability for an incident photon traversing a medium of thickness d can be written $1.-\exp(-d/f(E))$; the absorption mean free path $f(E)$ is a function of the photon energy E. It is plotted for both xenon and argon gas in Figure 4 and can be seen to increase a factor of four as the photon energy increases over the xenon K shell egde at 34.6 KeV [11]. The most probable energy described for the case of a 10 GeV electron radiating in M3 lay just under this threshold. Photons with higher energies, more probable from higher energy electrons, were less likely to convert. The absorption mean free path for an average energy photon emitted by a 10 GeV electron was 18 cm, corresponding to an absorption probability of approximately 10% in the 2 cm thick region of xenon in the xenon chamber.

The range R of a photoelectron in xenon is a strong function of the photoelectron energy E ($R \propto E^{1.75}$). It varies from 0.3 mm for a 6 KeV photoelectron to greater

than 6 mm for photoelectrons ejected with an energy greater than 40 KeV. The details concerning the channels available in the photoelectric process for an incident x-ray in xenon are reviewed by Bateman [12].

2.4.2 The Xenon Chamber

The xenon chamber was a multi-wire proportional chamber containing two vertical planes of parallel sense wires. Each plane consisted of 320 25 μm diameter gold plated tungsten wires spaced 2 mm apart. A central cathode plane with 192 parallel horizontal wires was located midway between the sense planes. Another plane of vertical cathode wires was located on the other side of each sense plane. The cathode planes consisted of 64 μm diameter Be-Cu wires spaced 1 mm apart in the two vertical planes and 4/3 mm apart in the central cathode plane. The cathode planes were all held at a potential of -3500 volts. The five planes in the chamber were located 4.8 mm apart.

The amplification of a pulse on a vertical sense wire and the induced pulse on a horizontal cathode wire was performed by electronics similar to the MWPC electronics already described. Every wire in the sense planes and each of the 64 sets of three adjacent wires in the central

cathode plane was connected to an amplifier circuit with an 800 μV threshold. The 64 channels for the central cathode plane effectively represented a plane of horizontal cathode wires spaced 4 mm apart. These channels were encoded for retrieval in the same manner as the twelve MWPC sense wires. The data corresponding to the active wires in the two sense planes were read, encoded and stored by the Xenon Data Processor.

The detection of a charged particle or an x-ray photon was complete when the latch corresponding to a given amplifier channel was set by the arrival of a special ST pulse at the xenon chamber. This pulse was 50 ns wider than the equivalent pulse sent to the six MWPC's in the magnetic spectrometer to ensure that the signals resulting from the short range photoelectrons ejected from xenon atoms by any incident x-rays were detected, in addition to the signals from the locations where the incident charged particles passed through the chamber.

2.4.3 The Helium Bag

Conversions of the emitted x-ray photons upstream of the xenon chamber were reduced by inserting a helium-filled polyethelene bag in the gap of the analyzing magnet M3.

The downstream end of the helium bag was cut off, and the bag was mounted to the upstream face of the xenon chamber. Two 25 μm thick mylar windows separated by 5 mm of air comprised the interface between the gas mixture in the chamber, consisting of xenon gas bubbled through liquid methylal at 0°C , and the helium contained in the bag. The helium was used to push the windows towards the upstream cathode plane to minimize the amount of xenon available for incident x-ray conversions in the space between the window and the cathode plane. An x-ray conversion was more likely to be detected when it occurred in the 2 cm of xenon between the vertical cathode planes.

2.4.4 Patterns from Synchrotron Radiation

The signature of an incident charged particle passing through the xenon chamber was an active wire at the same location in both sense planes. The pattern expected from a non-leptonic lambda decay with two charged decay products was thus two incident charged particle signatures in the chamber. This is illustrated in Figure 5a.

The x-ray photons emitted by an electron as it radiated in the magnetic field of M3, arrived at the active area of the xenon chamber in a region bounded in the

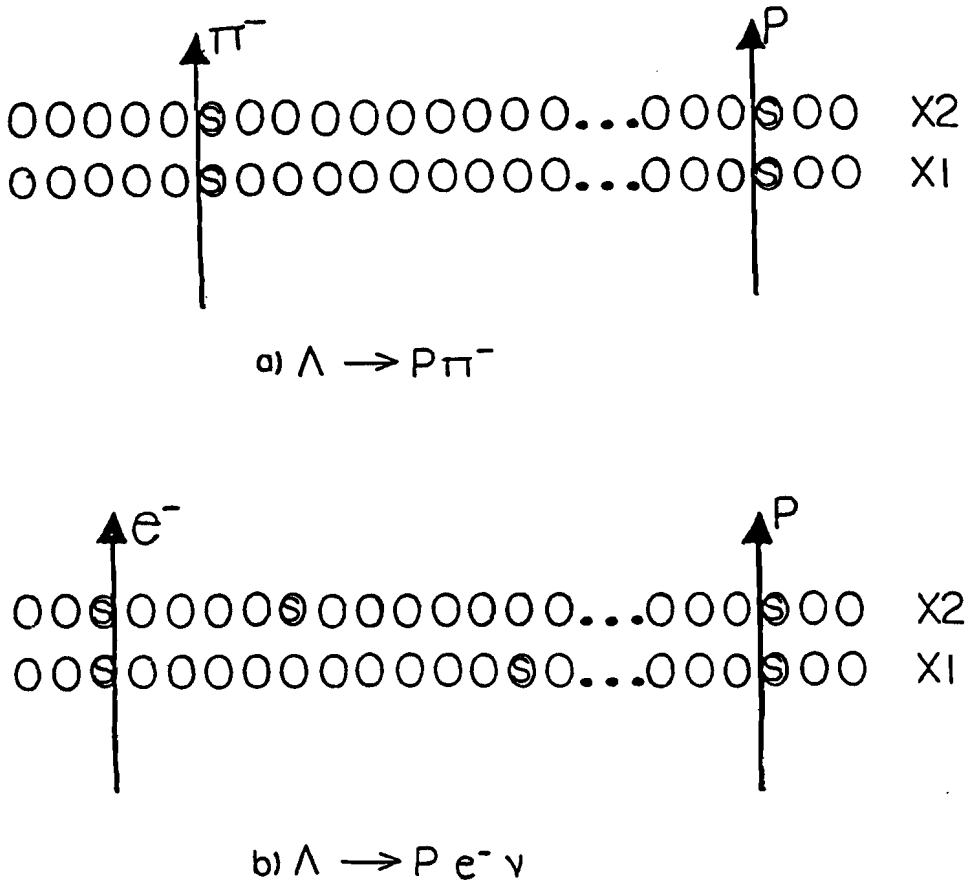

Figure 5. Xenon Chamber Sense Plane Patterns

$\hat{x}$ direction by the location of the deflected electron as it passed through the chamber, and the intersection with the tangent to the electron track at the entrance to M3. The position and size of this photon conversion region changed for each electron trajectory in the magnetic spectrometer. In addition, the electron remained undeflected in the $\hat{y}$ direction so the photons intersected the xenon chamber at the same location in the vertical dimension as the incident electron. All of this information was incorporated into the requirements of the electron signature defined for the offline analysis, which is described in Section 4.3.

A short range photoelectron resulting from the conversion of an incident x-ray photon appeared as a signal on a wire in just one of the sense planes at a given wire location, depending on how far into the xenon the photon traveled before the conversion. The pattern for a lambda beta decay, with an incident electron and proton passing through the chamber, is illustrated in Figure 5b. In this example there are also two x-ray photons detected by the sense planes. The manner in which the Xenon Data Processor triggered the experiment on such a pattern is described in Chapter 3.

2.5 The Lead Glass Array

The lead glass array, denoted PBG in Figures 1 and 2, was placed just downstream of C5 to intercept the negatively charged particle. In contrast to an incident hadron, an electron initiated a rapidly developing electromagnetic shower as it entered the lead glass blocks; this cascade of electrons and photons occurred because bremsstrahlung and pair production are the dominant interaction processes for relativistic electrons and photons. The intensity of the Cerenkov radiation emitted along the integrated path length of all the leptons in such an electromagnetic shower is proportional to the incident electron energy, and was detected by photomultiplier tubes viewing the transparent blocks.

Sixty four lead glass blocks, each 10 cm x 10 cm x 39 cm, were arranged with their long axes vertical in an array which was eight blocks wide and eight blocks deep; the configuration is illustrated in Figure 6. The upstream face of the array was 4.6 m downstream of the M3 exit aperture. It was centered vertically on the neutral beam position and was large enough in this dimension ($\hat{y}$) to intercept any negatively charged particle originating in the decay region which passed through the limiting aperture

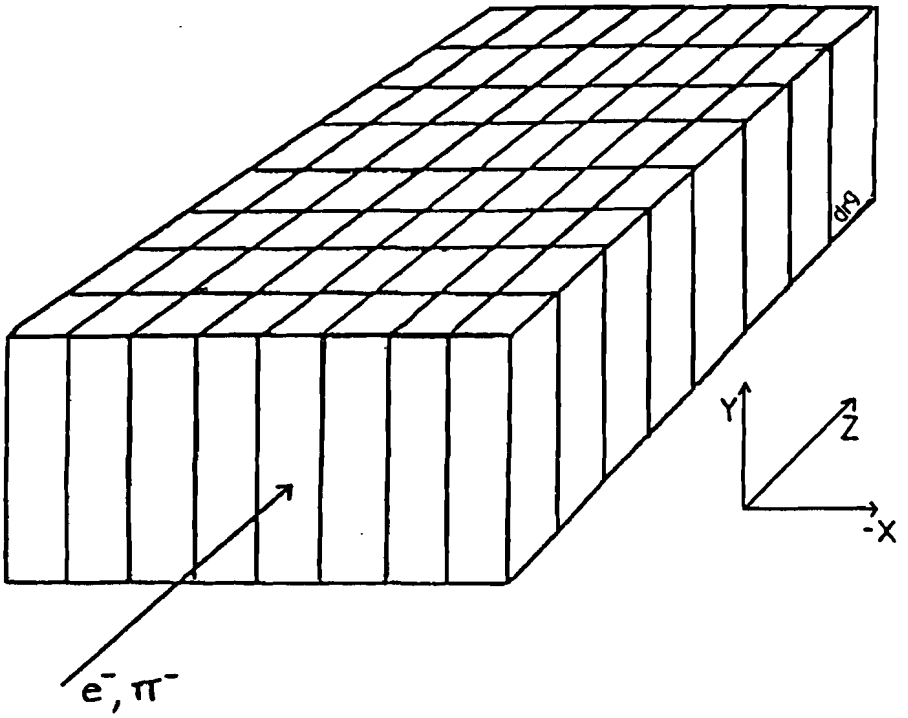

Figure 6. Lead Glass Configuration

of the analyzing magnet M3. The edge of the array was located 4 cm from the neutral beam axis ($+\hat{z}$) in the $+\hat{x}$ direction to ensure that the neutron and photon components of the neutral beam, which was 3 cm in radius at the array position, did not strike the detector.

The blocks were type SF2 glass with a 32 mm radiation length (X_0). The electromagnetic shower develepment was sampled every 3.1 X_0 and contained in a total of 25 X_0. Each block was wrapped with aluminum foil and viewed by a 4 cm diameter RCA 6342/V1 phototube centered on the 100 cm^2 face on top of the block. The high voltage for each tube, typically -1500 volts, was chosen so that all the phototubes gave the same response to a simulation of a fixed energy deposition in a single test block. The light for the simulation was provided by a neon flash lamp which sent light to the test block through a fiber optics light guide. Four other flash lamps, each servicing sixteen of the blocks through fiber optics connections, provided an online monitor of the phototube responses. The entire detector was air conditioned and housed in a steel box composed of removable 7 mm thick steel plates which provided magnetic shielding.

The anode signal from each phototube, typically 30 ns wide, was attenuated by 12 db and sent to one of the

channels of a 10-bit analog-to-digital converter (ADC). The ADC integrated the current and digitized the resulting charge. The attenuation was chosen to keep the charge within the 256 pc range of the ADC. This information was then retrieved by the data acquisition system for each event to be studied offline. The manner in which the digitized charge was converted into a measurement of the energy deposition in a corresponding lead glass block is discussed in Chapter 4.

The phototube output dynode signals from a selected portion of the array were used to form three prompt pulses which were combined in the electron trigger logic described in the next chapter.

2.6 The Threshold Cerenkov Counter

A 12 m long, 1.5 m diameter threshold Cerenkov counter filled with air, denoted CER in Figures 1 and 2, was placed between C5 and C6 to intercept the positively charged particle in a neutral vee event. A quartz face 5 cm diameter RCA 31000M phototube with high photocathode efficiency detected the Cerenkov radiation which was emitted by the positively charged particle and reflected by a tilted 1 m focal length mirror. The long axis of the

counter was aligned with the nominal direction of the daughter proton beam from lambda decays. The material from the mirror and back aluminum cover on the counter contributed 4% of a radiation length to the material in the path of the beam upstream of C6.

A threshold velocity β_o was set to discriminate protons from pions by altering the index of refraction of the air inside the counter according to $(n-1) = (n_A-1)P$, where P was the air pressure in atmospheres. The difference between the index of refraction of air at one atmosphere (n_A) and unity is 2.73×10^{-4}. A charged particle with velocity βc would then radiate if $\beta > \beta_o = 1/n$. The air pressure in the tank was chosen to be 0.06 atmospheres corresponding to a threshold momentum of 160 GeV/c for a proton and 24 GeV/c for a charged pion. Relativistic positrons, which were a consequence of pair production by the neutral beam, were also tagged in this manner.

The anode signal from the phototube was passively split into two signals, one of which was sent to an ADC channel and the other to a threshold discriminator. The discriminator output pulse was used in the trigger logic and also recorded in a coincidence register channel.

2.7 Positron Identification

Additional positron suppression was obtained by placing a two radiation length thick piece of lead followed by a scintillation counter, the combination denoted E1, at the downstream end of the spectrometer to intercept the positively charged particle. The scintillation counter sampled the electromagnetic shower originating in the lead. The anode signal from the phototube viewing the scintillation counter was sent to an ADC channel.

CHAPTER 3

TRIGGER REQUIREMENTS AND DATA ACQUISITION

3.1 The Neutral Vee Trigger

An effective trigger signature for the lambda charged decays $\Lambda \rightarrow p e^- \bar{\nu}_e$ and $\Lambda \rightarrow p \pi^-$, without any particle identification, was set up with coincidence logic units. In logical notation, this was written

$$V = \overline{S1} \cdot C1 \cdot C5P \cdot S2 \cdot C6 \cdot S3 \cdot \overline{S4} ,$$

where a dot(bar) indicates a logical AND(NOT). The C's denote the MWPC hodoscope elements already described. The S's refer to the output pulses from the threshold discriminators receiving analog signals from the phototubes

viewing the scintillation counters, the locations and sizes of which are illustrated in Figures 1 and 2. This trigger required two oppositely charged tracks to originate in the decay region between S1 and C1. A high momentum positive particle was characteristic of the lambda charged decays, in which the massive proton carries most of the parent lambda momentum.

The trigger rate reflects the effect of employing the neutral vee trigger. The beam delivery system typically provided 5×10^{9} incident protons at the production target during an accelerator pulse. The corresponding charged particle flux in the upstream MWPC's of the magnetic spectrometer was 5×10^{5}. There were 5500 V triggers from such a beam spill.

3.2 The Lambda Beta Decay Trigger

The trigger selecting lambda beta decays used the available particle identification to supplement the V trigger requirements. Both of the electron detectors contributed to this trigger. The dynode signals from the phototubes viewing the lead glass blocks were used to form the contribution from the lead glass array. The formation of this pulse, denoted ES, is discussed in Section 3.2.2.

The synchrotron radiation detector contributed to the trigger by requiring that the active sense wires in the xenon chamber formed a pattern consistent with the detection of synchrotron radiation. The Xenon Data Processor made this decision, denoted SR. The requirements of the synchrotron radiation trigger and the operation of the Xenon Data Processor are described in Section 3.3. Finally, a proton was selected by demanding the absence of an output pulse from the threshold discriminator receiving the signal from the phototube viewing the threshold Cerenkov counter. This pulse was denoted TCC. The lambda beta decay trigger was thus written

$$LB = V \cdot ES \cdot SR \cdot \overline{TCC} \ .$$

3.2.1 Implementation and Design Considerations

The complete lambda beta decay trigger was implemented in two stages, which are illustrated schematically in Figure 7. The first stage employed a fast trigger to reduce the rate handled by the much slower Xenon Data Processor, denoted XDP. The second stage involved a decision by the Xenon Data Processor, which controlled the

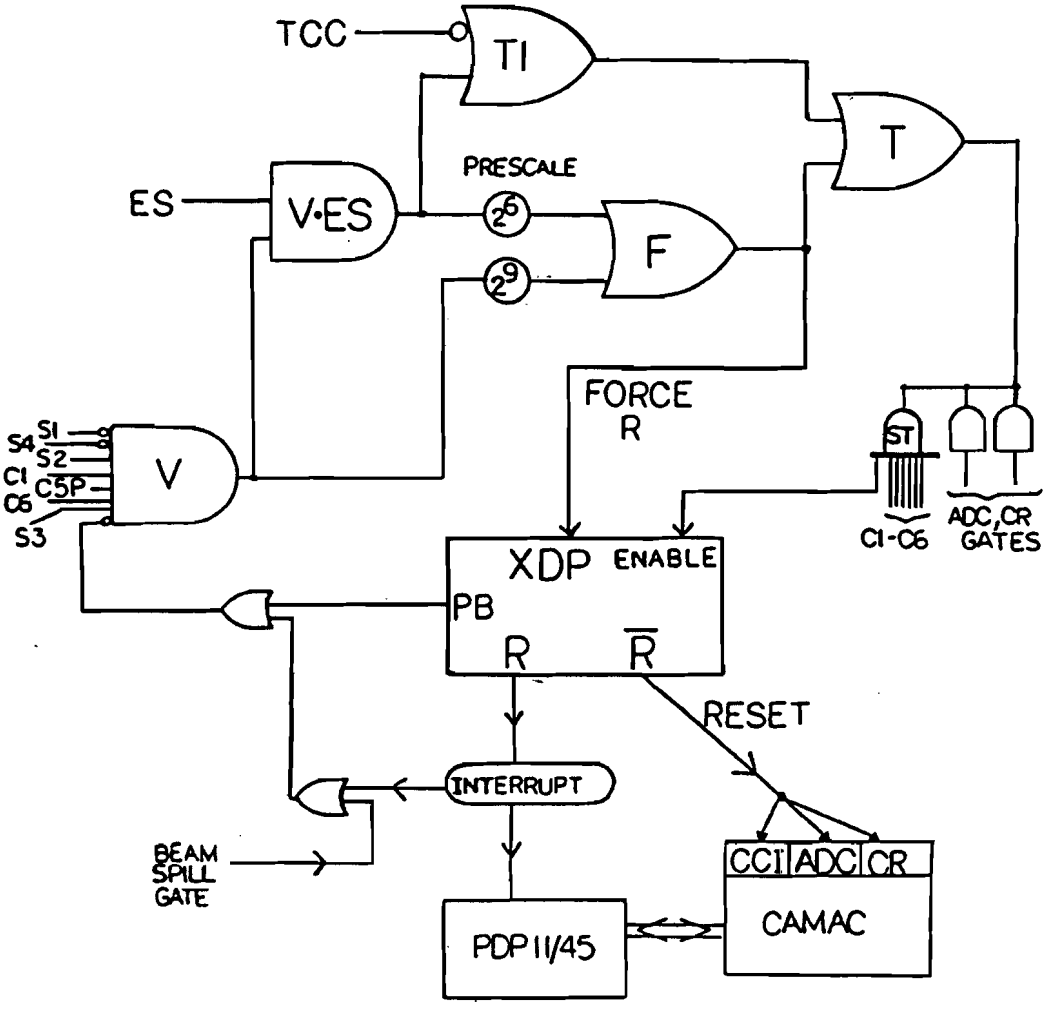

Figure 7. Trigger Logic and Data Acquisition

access of the data acquisition system to the spectrometer data.

The fast trigger used contributions from the lead glass array and the threshold Cerenkov counter to supplement the V trigger requirements. Fast coincidence logic units were used to form the logical combination $T1=V \cdot ES \cdot \overline{TCC}$ in less than 150 ns. This reduced the V trigger rate by a factor of nine; there were 590 T1 triggers from the typical beam spill discussed in Section 3.1. The ES requirement was responsible for a factor of five in this initial suppression. The xenon chamber data for the remaining events were then examined by the Xenon Data Processor. The V trigger was gated off during the operation of the Processor by a Busy signal, denoted PB in Figure 7. A decision was made in 16 μs. A positive response, denoted R, was generated by the Processor when the requirements of the synchrotron radiation trigger (SR) were satisfied by the event. This resulted in the retrieval of the spectrometer information by the data acquisition system. An additional suppression factor of eight in the trigger rate was provided by the SR requirement; there were 70 events satisfying the complete lambda beta decay trigger from the typical beam spill under discussion.

This experiment required a sample of events to which the lambda beta decays from the final sample could be normalized for the branching ratio measurement. An understanding of the electron identification efficiency and hadron rejection obtained with the electron detectors was also desired. These demands were met by mixing two other triggers, each reduced by a factor of 2^n by a prescaler, with the T1 trigger in the first stage of the trigger logic. The result of the first stage of the trigger was thus the T trigger, written

$$T = V \cdot ES \cdot \overline{TCC} + V/2^9 + V \cdot ES/2^6 \quad ,$$

where the "+" denotes a logical OR. The prescaled V trigger (n=9) component provided a sample of non-leptonic lambda decays ($\Lambda \rightarrow p\pi^-$) which could be used for the normalization. The logical combination V•ES (n=6) enriched the electron pair event contamination in the V trigger and was useful for calibration purposes. Both prescaler outputs were sent to coincidence register channels in order to flag the events in the offline analysis described in the next chapter.

A T trigger resulted in preparations for the possible retrieval of the spectrometer data by the data acquisition system. Gates were sent to both the ADC's and the

coincidence registers to store the appropriately delayed event information. The ST pulses were sent to the MWPC electronics to set the amplifier channel latches corresponding to the active sense wires. The wire hit data from the xenon chamber were also latched, at which point the operation of the Xenon Data Processor was initiated.

The failure of the xenon chamber data to satisfy the synchrotron radiation trigger requirements prompted the Processor to issue a negative response, denoted $\overline{R}$, which cleared the spectrometer data and released the V trigger logic, unless one of the prescaled triggers had been satisfied. A prescaled trigger forced the Processor instead to generate an R response to ensure that the retrieval of the spectrometer data proceeded regardless of outcome from the SR decision logic in the Processor. A pulse from an OR circuit combining the two prescaled triggers, denoted F in Figure 7, informed the Processor that the event to be examined was a prescaled trigger.

3.2.2 The Contribution from the Lead Glass Array

The trigger used to select events with an electromagnetic shower in the lead glass array was formed by combining the phototube dynode signals from various

portions of the lead glass array. The formation of the three prompt pulses used in the trigger logic is illustrated in Figure 8. The phototube signals corresponding to the 32 blocks in the front four rows of the array were summed by a set of linear fan-in modules to form a single signal. This signal was discriminated at two different thresholds corresponding to a low energy deposition of 6 GeV, denoted L, and a higher energy deposition of 11 Gev, denoted H. The third pulse, denoted B, represented an energy deposition of 1 GeV in the final two rows of the array. It was formed by discriminating the summed output dynode signals of the last two rows in the array in a similar fashion. These three pulses were then arranged in coincidence logic circuits to form the logical combination $ES = L \cdot (\overline{H} \cdot B)$, which is outlined schematically in Figure 8.

The ES trigger logic required a minimum energy deposition of 6 GeV in the initial 12.4 X_o of the array, an energy threshold which corresponded to the lowest energy electrons from lambda beta decays entering the array. It allowed an energy deposition of greater than 1 GeV in the final 6.2 X_o of the total 25 X_o comprising the detector only if a large amount of energy, at least 11 GeV, was deposited in the front. This supplemented the already effective rejection of low energy pions with rejection of

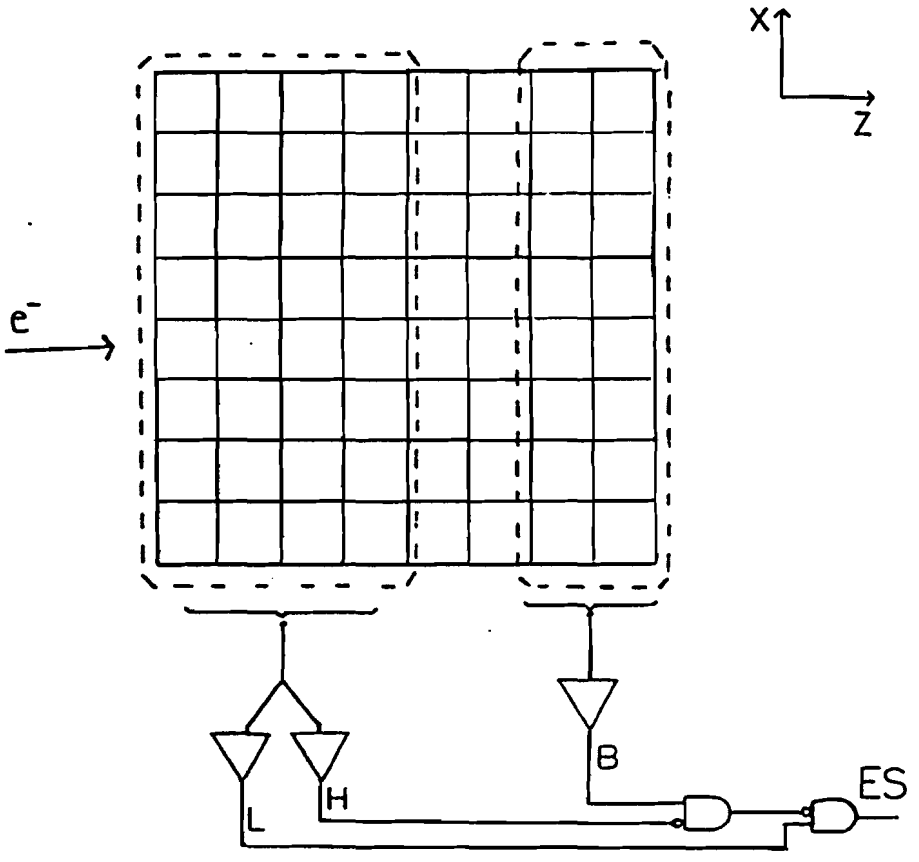

Figure 8. ES Trigger Logic

higher energy pions which reached only the low energy threshold in the front and deposited what for an electron would be too large an amount of energy in the back of the array.

3.3 The Xenon Data Processor

The Xenon Data Processor was an emitter-coupled logic device built to retrieve, encode and store the identity of the active xenon chamber sense wires. The data from the two vertical sense planes were compared by the Processor to determine if synchrotron radiation had been detected in addition to the charged particles from a two track event. The sense plane signatures of both synchrotron radiation and incident charged particles have been described in Section 2.4.4; at a given wire location, synchrotron radiation appeared as an active wire in just one of the sense planes. In contrast, an incident charged particle passing through the chamber left an active wire in both sense planes at a given wire location. The Processor was thus designed to compare the two sense wires at each wire location. The operation of the Processor is sketched in Figure 9; the abbreviations used there will be defined below.

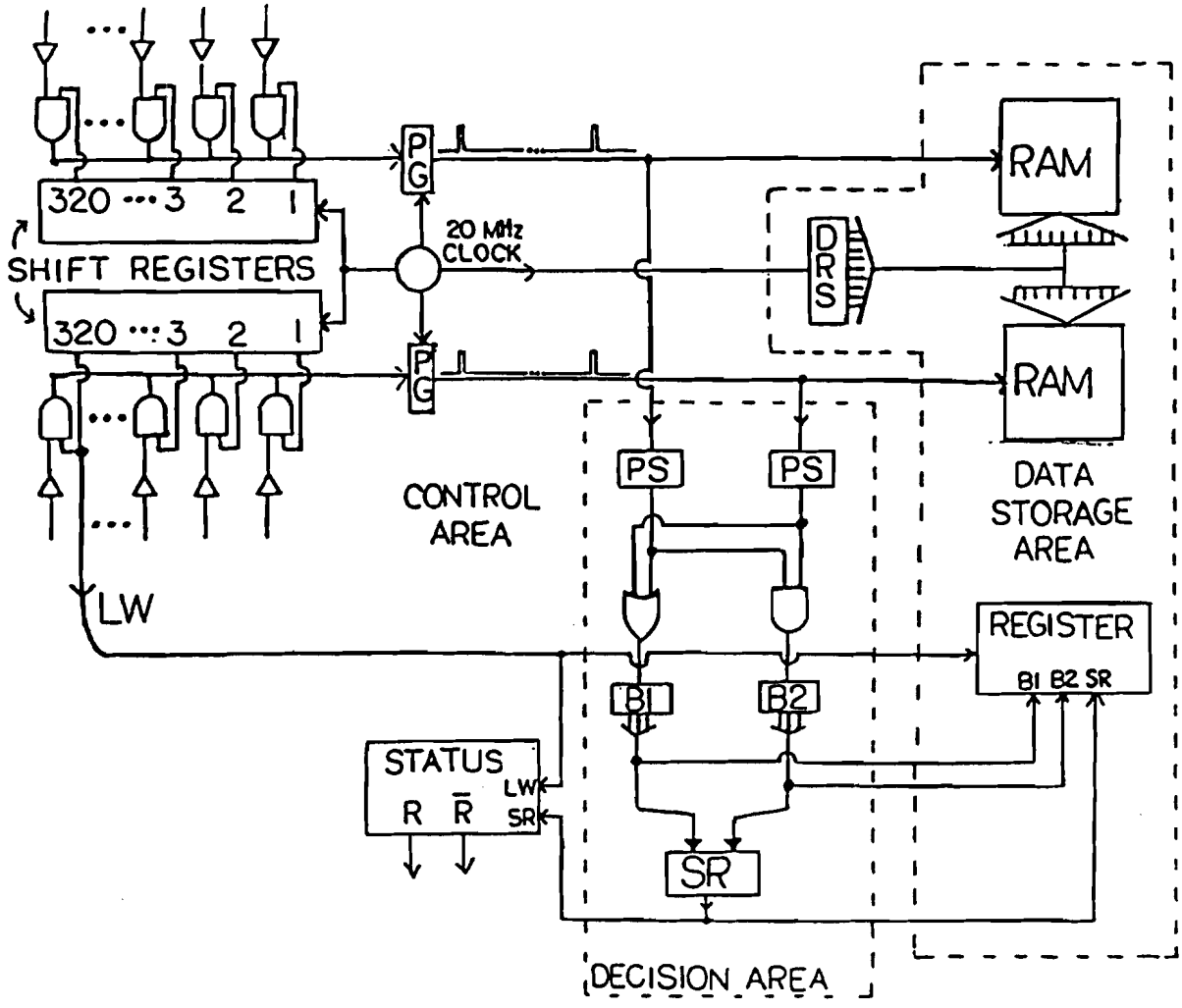

Figure 9. Xenon Data Processor Operation

The Processor retrieved the data from the two sense planes simultaneously. Every 50 ns, the amplifier channel latches corresponding to the two wires at one of the wire locations in the sense planes were examined. The 320 wire locations were examined sequentially so the entire retrieval process lasted 16 μs. A 20 ns pulse was generated by the pulse generation (PG) circuits when an active sense wire was found in one of the sense planes. The data from each sense plane was thus converted into a sequence of pulses; the time a given pulse was generated was a function of the position an active wire occupied in the sequence of 320 wires comprising each sense plane. An example of these two sets of pulses is sketched in Figure 9. The pulses shown emerging from the PG circuits correspond to the sense plane pattern for the non-leptonic lambda event example illustrated in Figure 5a.

The two sets of pulses representing the data in the sense planes were sent to the decision area, where the width of the pulses was modified in pulse stretching (PS) circuits. A pulse corresponding to an active sense wire was stretched in time to overlap the pulse that would have been formed if the next wire to be examined had detected a signal. Adjacent active wires in a given sense plane were thus merged into one pulse. A logical comparision between the two sets of modified pulses was then performed. The

logical OR's and the logical AND's incremented a pair of binary counters, respectively labelled B1 and B2 in Figure 9.

A logical AND corresponded to an incident charged particle passing through the chamber. The ideal sense plane pattern expected when this occurred consisted of an active wire in each sense plane at a given wire location. The pulse stretching ensured that a comparison between two active wires at adjacent wire locations in different sense planes would also form a logical AND. Since any logical AND was also a logical OR, both B1 and B2 were incremented by a logical AND. As an example, the non-leptonic lambda event pictured in Figure 5a resulted in two counts in B2 (AND's) and two counts in B1 (OR's).

A lambda beta decay was distinguished from the non-leptonic lambda events by the presence of additional counts in B1. An additional logical OR was the signature of a photoelectron, which, after being ejected from a xenon atom by an incident x-ray photon, had been detected in only one of the sense planes at a given wire location. The synchrotron radiation (SR) trigger logic, employing three magnitude comparators and a pair of subtractors, used the binary outputs of B1 and B2 to require that an event contain at least one such additional logical OR. In

logical notation, the requirements of the synchrotron radiation trigger were written

$$SR = (B1-B2 \geq 1) \bullet (B1 \geq 3) \bullet (B2 \leq 5) \ .$$

The last requirement was used to remove multiple charged track events from consideration. The lambda beta decay illustrated in Figure 5b is an example of an event satisfying all three requirements; four counts were accumulated by B1, and two counts were accumulated by B2.

At the same time that the two sets of pulses generated by the PG circuits were being compared in the decision area, a scaler in the data storage area was incrementing so that its output corresponded to the binary number of the most recently examined wire location. This nine-bit Data Reconstruction Scaler (DRS) was incremented each time a different wire location was examined. When an active wire was found in one of the sense planes, the contents of the scaler was entered into a random access memory (RAM). There was a RAM corresponding to each sense plane; each RAM was used to store up to fifteen nine-bit words in an event.

A Last Wire (LW) pulse was generated after all the wires in the sense planes had been examined. The binary outputs of B1 and B2 were then loaded into a register which

was located in the data storage area of the Processor. One bit in the register was set if the SR trigger logic had been satisfied; the register thus contained the information necessary to monitor the performance of the Processor for each event. The final Processor status was also released at this time. As discussed in Section 3.2.1, an R response was issued when an event satisfied the SR trigger logic, and the spectrometer data was subsequently retrieved by the data acquisition system. An R response was also issued for any prescaled event which initiated the Processor operation. An $\overline{R}$ response was issued for any T1 trigger failing to satisfy the SR trigger requirements; the spectrometer data was subsequently reset for such an event.

3.4 Data Acquisition

A conventional CAMAC/PDP11 system was used to retrieve the elements of the event record from the spectrometer and store them temporarily on a high speed disk. A priority interrupt was sent to the computer to initiate the read sequence for an event when an R response was issued by the Xenon Data Processor. The V trigger remained gated off until the retrieval was complete. The encoded wire numbers corresponding to the amplifier channel latches set for the MWPC sense planes and xenon chamber central cathode plane,

the binary numbers stored in the two Processor RAM's , and the data in the Processor Register were serially retrieved by a CAMAC-chamber interface module, denoted CCI in Figure 7. The data words coresponding to the ADC and coincidence register channels were then entered into the event record. The entire retrieval of an event typically lasted almost 800 μs. In the case of an $\overline{R}$ response, the Processor Busy signal was released after a 1 μs delay to allow the $\overline{R}$-initiated clear to reset the data for the entire spectrometer in preparation for the next V trigger.

Each beam spill lasted 800 milliseconds and was repeated about every 12 seconds; the data acquisition rate was typically 85 events with 5×10^9 protons incident on the production target. Higher intensities were undesirable because of the substantial accidental rates in the counters, although the system was capable of handling 400 events per spill.

The conclusion of the beam spill required the computer to read the data accumulated in twenty scalers monitoring the rates in several counters and the number of events satisfying various trigger conditions. The incident proton beam intensity measured by the ionization chamber upstream of the production target was also recorded. Alternate spill records contained either the offset (pedestal) of the

ADC channels or the response of the phototubes in the lead glass array to the light pulser system.

The information on the disk was written onto 800 BPI magnetic tape between beam spills. Separate on-line software enabled such diagnostic histograms as wire hits in the proportional chambers and counts in the ADC channels to be displayed on a storage oscilloscope while the data was accumulating.

Roughly 150 data tapes,each containing 65,000 triggers, were written during the months of Sept.-Oct. 1979. The LB triggers constituted 70% of the events written to tape. They form the data set from which the final sample of lambda beta decays was chosen. The prescaled triggers comprised the remainder, with the prescaled V triggers contributing 10% of the total events recorded. The preceding three months involved calibration and trigger tests necessary in setting up conditions for the smooth operation of the experiment.

CHAPTER 4

EVENT SELECTION

4.1 Event Reconstruction

4.1.1 MWPC Alignment

The initial step in the reduction of the raw trigger events to the final lambda beta decay sample was the reconstruction of charged particle trajectories in the spectrometer using the MWPC wire hit data. This required knowledge of the relationship between the locations of the wires in the MWPC sense planes and the coordinate system defined in Section 2.2. The horizontal and vertical sense

plane wires were parallel to the x and y axes of this coordinate system. The positions of the sense planes along the z axis were measured several times during the experiment. The only other requirement was to determine the intersection of the z axis with each of the sense planes. This information was obtained by removing the production target, turning off all the magnets, directing the incident proton beam at a reduced intensity through the collimator and triggering on the coincidence between scintillation counters placed in the undeflected proton beam at the upstream and downstream ends of the spectrometer.

4.1.2 Pattern Recognition

The pattern recognition software searched for events satisfying the neutral vee topology. The y coordinates were fit with straight lines using the least squares technique. A calculation of the difference between the slopes of line segments drawn through the x coordinates in planes upstream and downstream of the analyzing magnet M3 which met at the center of the magnet provided the deflection in the known M3 magnetic field integral, constituting the momentum measurement of each charged particle. The intersection of the two tracks upstream of

M3 provided the decay vertex.

Approximately 80% of the V triggers were successfully reconstructed. This percentage dropped to 50% for the LB triggers. The SR (synchrotron radiation trigger) requirement had a tendency to pick out multiple charged track events that were uninteresting and unreconstructable.

The momentum components of the two charged particles and the decay vertex coordinates were written into a summary event record along with the error matrix associated with the geometrical fit to the neutral vee topology, the digitized charges from the ADC channels for phototubes with signals, the locations of all the active MWPC and xenon chamber sense wires, and the status of both the Processor Register and the coincidence registers. The summary event records were stored on thirty 6250 BPI magnetic tapes which were used in the subsequent analysis of the experiment.

All the reconstructed triggers on these data summary tapes were subjected to fiducial cuts which were slightly more restrictive than the real apertures in the spectrometer. The decay vertices were required to be inside the decay region. The MWPC wire hit data were used to remove events which contained an additional accidental track.

4.1.3 The Reconstructed Prescaled Triggers

The status of the latches in the coincidence register channels distinguished the prescaled triggers from the LB triggers stored on the data summary tapes. The 7.8×10^5 reconstructed events in the prescaled V trigger sample were primarily non-leptonic lambda decays ($\Lambda \rightarrow p\pi^-$), which were used to provide the normalization in the lambda beta decay branching ratio measurement and to monitor the performance of the apparatus. The invariant mass of the neutral parent was calculated assuming the $p(\pi^-)$ mass hypothesis for the positively (negatively) charged particle. Events with a mass which differed from the known lambda mass of 1115.57 MeV [2] by less than three standard deviations contributed to the non-leptonic lambda decay sample.

Calculations using other mass combinations revealed that the composition of the reconstructed V trigger sample was 63% $\Lambda \rightarrow p\pi^-$, 7% $K^0_S \rightarrow \pi^+\pi^-$ and less than 1% $\bar{\Lambda} \rightarrow \bar{p}\pi^+$ decays. The remaining events, which fit none of these mass hypotheses, were primarily a consequence of neutral beam interactions in the windows of the evacuated pipe in the decay region. Electron pair production accounted for 17% of these events. A reconstructed electron pair event was characterized by a small opening angle in the laboratory

between the electron and positron and a separation between the charged particle tracks only in the x-view downstream of the magnet M3. The electron pair events constituted five percent of the entire reconstructed V trigger sample.

The additional ES (electromagnetic shower trigger) requirement in the prescaled V•ES triggers enhanced the probability that the negatively charged particle was an electron. Twenty-five percent of the reconstructed prescaled V•ES triggers were electron pair events.

4.1.4 The Reconstructed LB Trigger Sample

The final sample of lambda beta decays was extracted from the 3.4×10^6 reconstructed LB triggers stored on the data summary tapes. A sample p-pi invariant mass plot for the reconstructed LB triggers is presented in Figure 10. The peak at the lambda mass indicates the amount of non-leptonic background to be rejected offline. The electron trigger had already provided a factor of 100 in non-leptonic rejection; this will be discussed in detail in Sections 4.2 and 4.3.

The Monte Carlo studies described in Chapter 5 indicated that the majority of the lambda beta decays

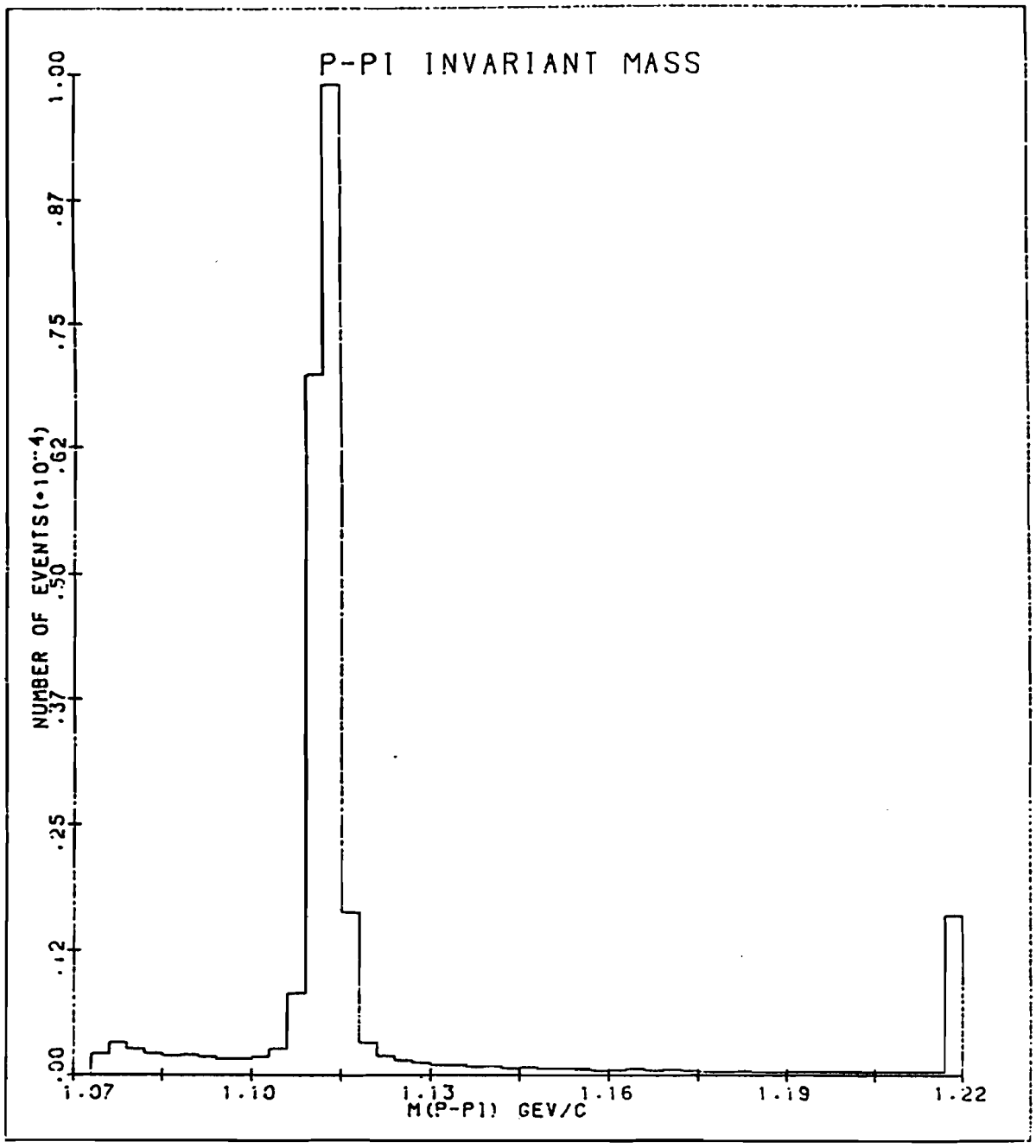

Figure 10. P-Pi Invariant Mass - LB Triggers

detected in the apparatus were populating the tails in this invariant mass distribution. Kinematic requirements and offline electron identification from the lead glass and synchrotron radiation detectors were used to extract the lambda beta decay signal from the data. The electron signature used in the offline analysis was constructed to maintain a reasonable detection efficiency for lambda beta decays, while concurrently maximizing the level of non-leptonic lambda rejection. The values quoted for such overall efficiencies always refer to the integrated spectra of both the electrons from lambda beta decays and the negatively charged pions from non-leptonic lambda decays entering the detectors unless otherwise specified.

4.2 The Lead Glass Array

4.2.1 Calibration

The first step in using the information from the lead glass array was to obtain a set of calibration constants, one for each ADC channel corresponding to a block in the array. This multiplicative constant converted the digitized charge from the event record into a measurement

of the energy deposition in each block. The total energy deposition and location of the electromagnetic shower induced by the incident negatively charged particle in a lambda beta decay candidate, as well as the longitudinal and transverse shower development, could be examined and the particle identity thus established.

The electron pair events from the data summary tapes provided a sample of momentum analyzed electrons which were used to continuously monitor the calibration constants during the course of the experiment. Each electron was projected to the array and the blocks contributing signals to the shower were determined. The calibration constants were found by using a least squares technique and minimizing the following expression:

$$\sum_i (P_i - \sum^N c_j q_j)^2 ,$$

in which P_i refers to the momentum of an incident electron and $c_j q_j$ is the unknown calibration constant multiplying the digitized signal from the j-th block in a shower with N contributing blocks. The calibration constants typically drifted less than 10% over the course of the experiment.

The calibration constants were corrected for an overall light attenuation of 8% over the length of the lead

glass blocks, measured by directing momentum analyzed electrons to intercept the blocks above and below the central region illuminated by the electrons from the reconstructed electron pair events on the data summary tapes. This was accomplished with a modification of the V•ES trigger in which the S1 contribution was replaced by the logical combination $\bar{A}\cdot B$, where A and B represented two scintillation counters separated by a thin piece of lead. The scintillator sandwich was placed in the neutral beam immediately downstream of the collimator exit. The charged particles from an electron pair originating in the lead were detected in B and subsequently deflected out of the neutral beam in the horizontal magnetic field of a dipole vernier magnet placed upstream of S1. The entire vertical face of the lead glass array shadowed by the limiting aperture of M3 could be illuminated by electrons as the strength of the magnetic field was adjusted.

4.2.2 Electron Identification and Hadron Rejection

An electron signature in the lead glass array was defined with several requirements. The total energy deposited in the shower, denoted E, was measured; the resolution $\sigma(E)$ obtained with the array was $\sigma(E)/E = 0.20/\sqrt{E}$. This total shower energy was required

to be a large fraction of the incident momentum (P) measured by the magnetic spectrometer. The momentum dependent lower limit for the required E/P ratio varied from 0.87 for P<10 GeV/c to 0.91 for P>25 GeV/c. The E/P values for a sample of 13.5 GeV/c electrons are plotted in Figure 11. There was another momentum dependent requirement on the longitudinal shower development; the fraction of the total shower energy deposited in the first two rows (6.2 X_o) was required to exceed a lower limit of 0.15 for P>25 GeV/c up to 0.25 for P<10 GeV/c. In addition, the transverse shower development was constrained so that at least 95% of the energy deposited in the shower was contained in the three columns closest to the incident charged particle projection at the array.

The ES trigger requirement performed part of the desired π-e discrimination. The online non-leptonic lambda rejection could be studied with the reconstructed V triggers by examining the status of the coincidence register channel corresponding to the ES trigger logic. The ratio of the total number of non-leptonic lambda decays to the number of these events which set the latch in the coincidence register channel was a measurement of the online trigger rejection, denoted Rj. The resulting rejection was a factor of seven. The variation of the

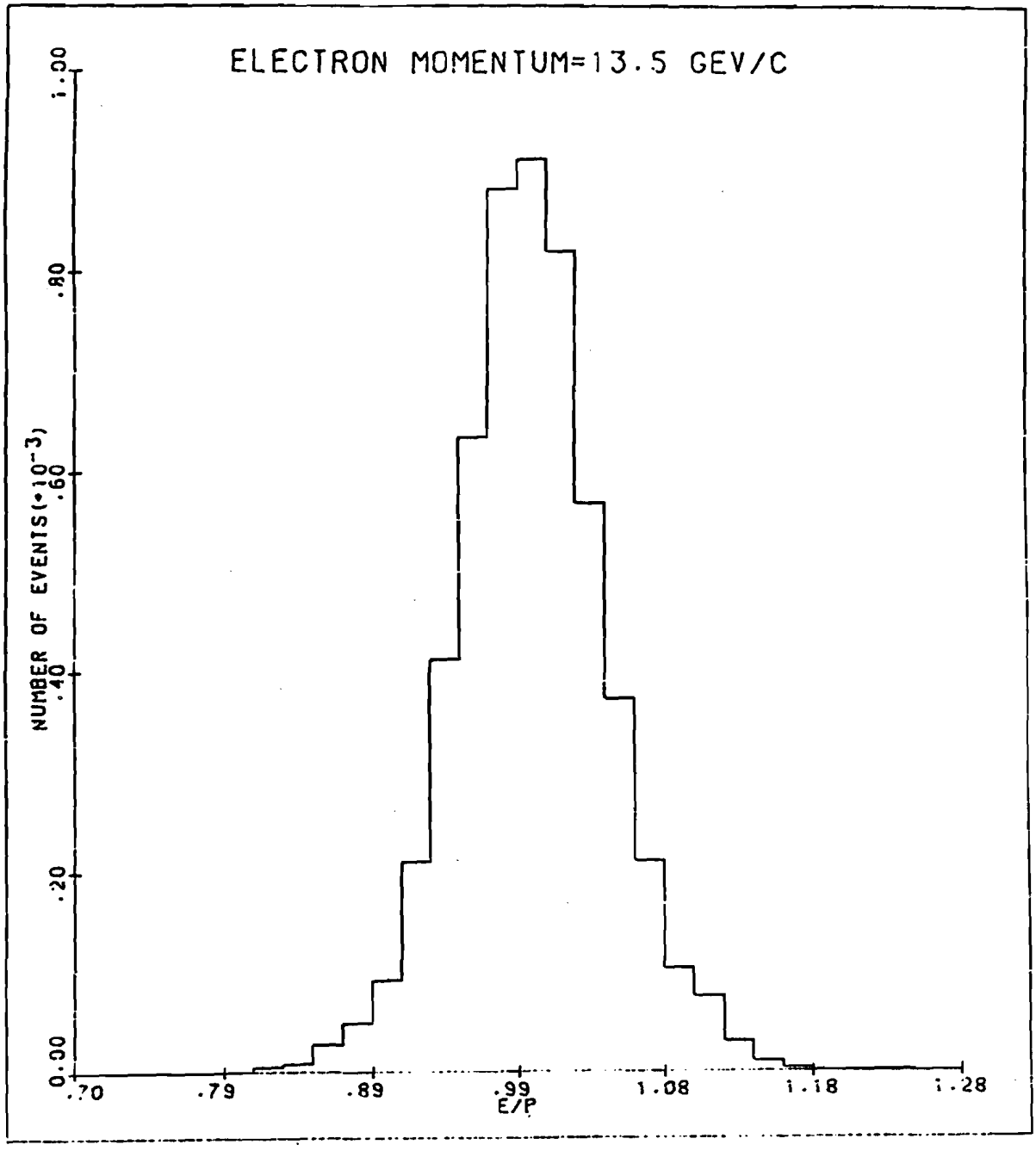

Figure 11. E/P Distribution - 13.5 GeV/c Electrons

rejection as a function of the incident pion momentum was:

P(GeV/c):	8.5	13.5	18.5	23.5	28.5	33.5	38.5
Rj:	25	10	6	6	5	4	3

The fact that the low momentum rejection was more effective was a consequence of the discriminator thresholds used in defining the ES trigger. The key observation is that the efficiency of the ES trigger for incident electrons, obtained from the electron pair data in the reconstructed V trigger sample, was measured to be greater than 98%.

The offline contribution to the total hadron rejection made use of the characteristics of the electron signature described above. The momentum dependent limits already quoted could be varied to change both the total non-leptonic lambda rejection and lambda beta decay efficiency. The values given correspond to a rejection factor of 145 with an efficiency of 96%. This was the signature used in defining the final data sample discussed in Section 4.7. The rejection could be raised (lowered) by tightening (relaxing) the electron signature requirements. The rejection (Rj) then varied with the efficiency (Ef):

Rj:	145	250	340
Ef:	0.96	0.91	0.86 .

4.3 The Synchrotron Radiation Detector

The wire hit data from the xenon chamber sense planes were used to identify the negatively charged particle in a lambda beta decay candidate as an electron by requiring the detection of synchrotron radiation. The wire hits in both the two vertical sense planes and the horizontal cathode plane were formed into clusters of adjacent wires. The two incident charged particles in a neutral vee event were projected to the chamber position, and the clusters located at the projections were identified; these were referred to as charged particle clusters. The x-ray cluster candidates in the sense planes were chosen from the remaining clusters by requiring them to be located in the appropriate photon conversion region (discussed in Section 2.4.4), which was calculated for each electron trajectory.

4.3.1 Electron Identification and Hadron Rejection

The SR trigger requirements rejected any event in which the only clusters detected in the sense planes were charged particle clusters. The online pion rejection and electron efficiency could be studied by examining the the state of the decision bit in the Processor Register for

reconstructed prescaled trigger samples of non-leptonic lambda decays and electron pair events. The total online rejection for non-leptonic lambda decays was a factor of 16, corresponding to an overall lambda beta decay efficiency of 80%. These quantities varied as a function of the incident negatively charged particle's momentum:

P(GeV/c):	8.5	13.5	18.5	23.5	28.5	33.5	38.5
Rj:	13	17	16	17	17	15	17
Ef:	0.84	0.83	0.79	0.79	0.74	0.74	0.68

The offline electron signature contributing to the total rejection required an event which had passed the SR trigger test to have at least one x-ray cluster candidate in either sense plane. The sense planes were allowed to contain only x-ray cluster candidates and charged particle clusters. This removed from consideration events with accidental clusters outside the calculated photon conversion region. In addition, the charged particle clusters and the x-ray cluster candidates were not allowed to consist of more than three adjacent wires. This electron signature, providing a total non-leptonic rejection factor of 70 with an electron efficiency of 71%, was used in selecting the events in the final sample of lambda beta decays.

The momentum dependence of the pion rejection and electron efficiency for these requirements was:

P(GeV/c):	8.5	13.5	18.5	23.5	28.5	33.5	38.5
Rj:	42	58	75	86	98	90	96
Ef:	0.76	0.75	0.70	0.69	0.64	0.64	0.60

This response demonstrated the expected drop in the synchrotron radiation detection efficiency at higher electron momenta, resulting from both the lower probability for a photoelectric conversion by the higher energy incident x-rays emitted by such electrons, as well as the smaller photon conversion region available to the stiffer electrons. The distribution for the fraction of the electrons (Fr) satisfying this electron signature, as a function of the number of x-ray cluster candidates detected (Nx), was:

Nx:	1	2	3	4	5	≥ 6
Fr:	0.28	0.29	0.21	0.11	0.07	0.04

The tail was primarily populated by the lower momentum incident electrons which emitted the photons with a higher conversion probability.

The non-leptonic rejection could be increased by

supplementing the electron signature criteria already described by other requirements on the characteristics of the set of x-ray cluster candidates. The non-leptonic lambda decays meeting the above electron criteria contained spurious clusters in the imaginary photon conversion region calculated at the chamber for the pion trajectory in the event. These clusters could not be attributed to the detection of synchrotron radiation from the pion. The events were used to charaterize the location and size of the spurious clusters, the source of which was often the material comprising the chamber. Both the ejection of an energetic knock-on electron by one of the incident charged particles from the event and accidental neutral beam interactions were responsible for the spurious clusters. The electron signature could be tightened to exclude these spurious cluster categories from the set of credible x-ray clusters.

The detection of the signals induced on the horizontal ($\hat{y}$) wires in the central cathode plane provided additional constraints for an electron signature. The x-ray photons arrived at the horizontal cathode wire cluster corresponding to the location of the incident electron as it passed through the chamber. Any clusters in the central cathode plane which were not charged particle clusters could be used to label an x-ray cluster candidate in the sense planes as spurious.

The overall lambda beta decay efficiency and non-leptonic rejection corresponding to these tighter electron signatures varied as follows:

Rj:	70	150	350
Ef:	0.71	0.63	0.45 .

The efficiency of the sense planes for detecting incident charged particles passing through the xenon chamber was 97-100%, obtained by measuring the fraction of the incident charged particles with a corresponding charged particle cluster. The efficiency for the central cathode plane was 74% for incident hadrons (protons and pions) and 94% for incident electrons satisfying the electron signature defined above, reflecting the additional contribution to the induced signal on a cathode wire from the photoelectrons associated with a radiating electron.

4.4 Other Particle Identification

The efficiency of the threshold Cerenkov counter for correctly tagging the positively charged particle in a neutral vee event was studied with the reconstructed

prescaled triggers. The status of the coincidence register corresponding to the TCC pulse used in the T1 trigger logic was examined for the non-leptonic $\Lambda \rightarrow p\pi^-$ and $K_S^0 \rightarrow \pi^+\pi^-$ decays, as well as electron pair events. Positrons were identified with 98% efficiency. The measured momentum dependence of the detection efficiency for protons and positively charged pions is illustrated in Figure 12. This corresponded to integrated efficiencies of respectively 0.83 and 0.07 for detecting Ke3 and lambda beta decays in the fiducial region defined for the analysis.

Additional positron identification was obtained by examining the ADC channel corresponding to the scintillation counter in E1. The pulse height distribution for hadrons is compared to the equivalent distribution for positrons in Figure 13. A large pulse height clearly distinguished the positrons. A requirement that an event had less than 800 counts removed 70% of the positrons and 8% of the protons.

4.5 The V Trigger Efficiency

The efficiency of the V trigger for detecting neutral vee events in the fiducial region of the spectrometer was studied by removing various elements of the apparatus from

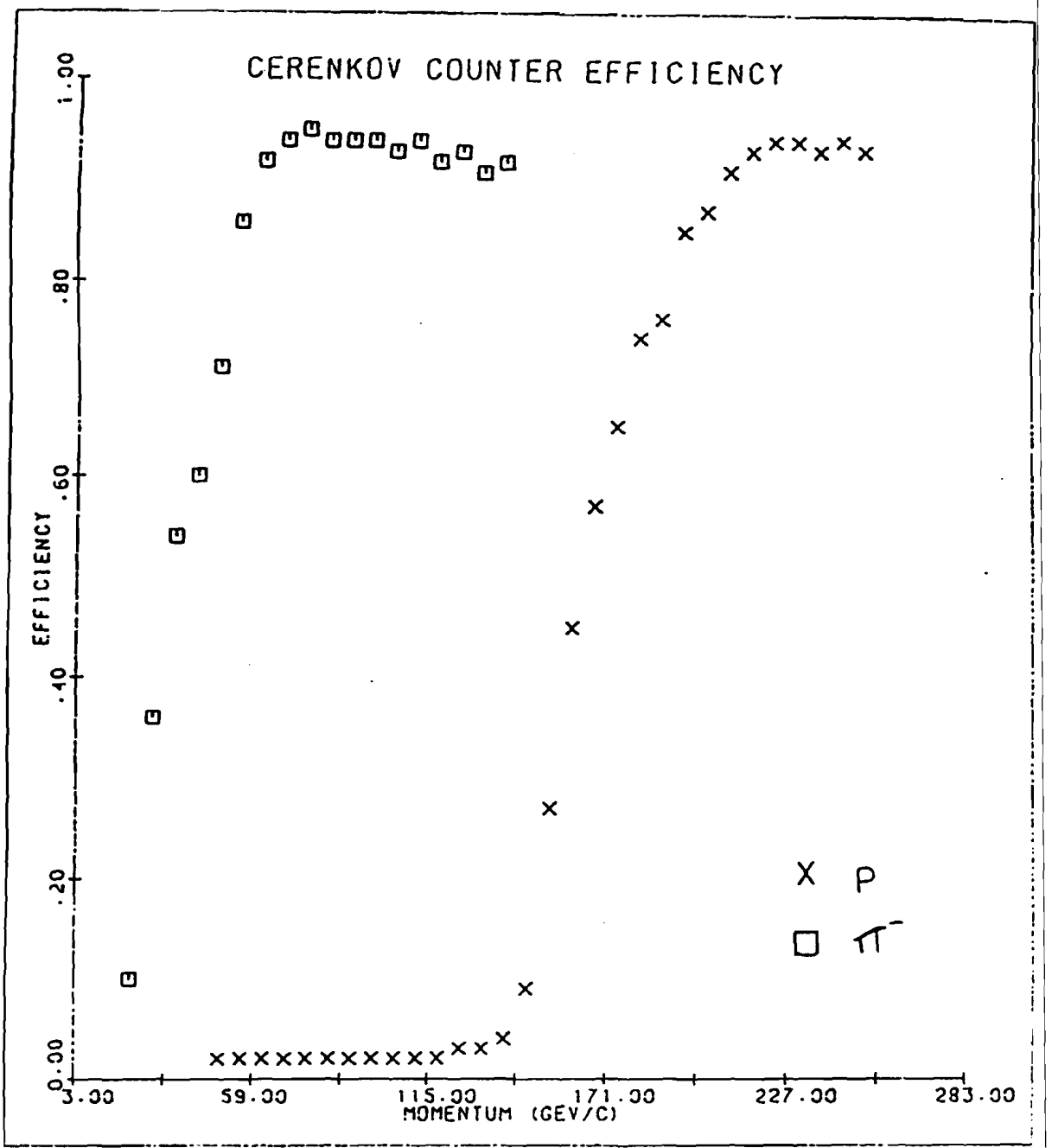

Figure 12. Cerenkov Counter Trigger Efficiency

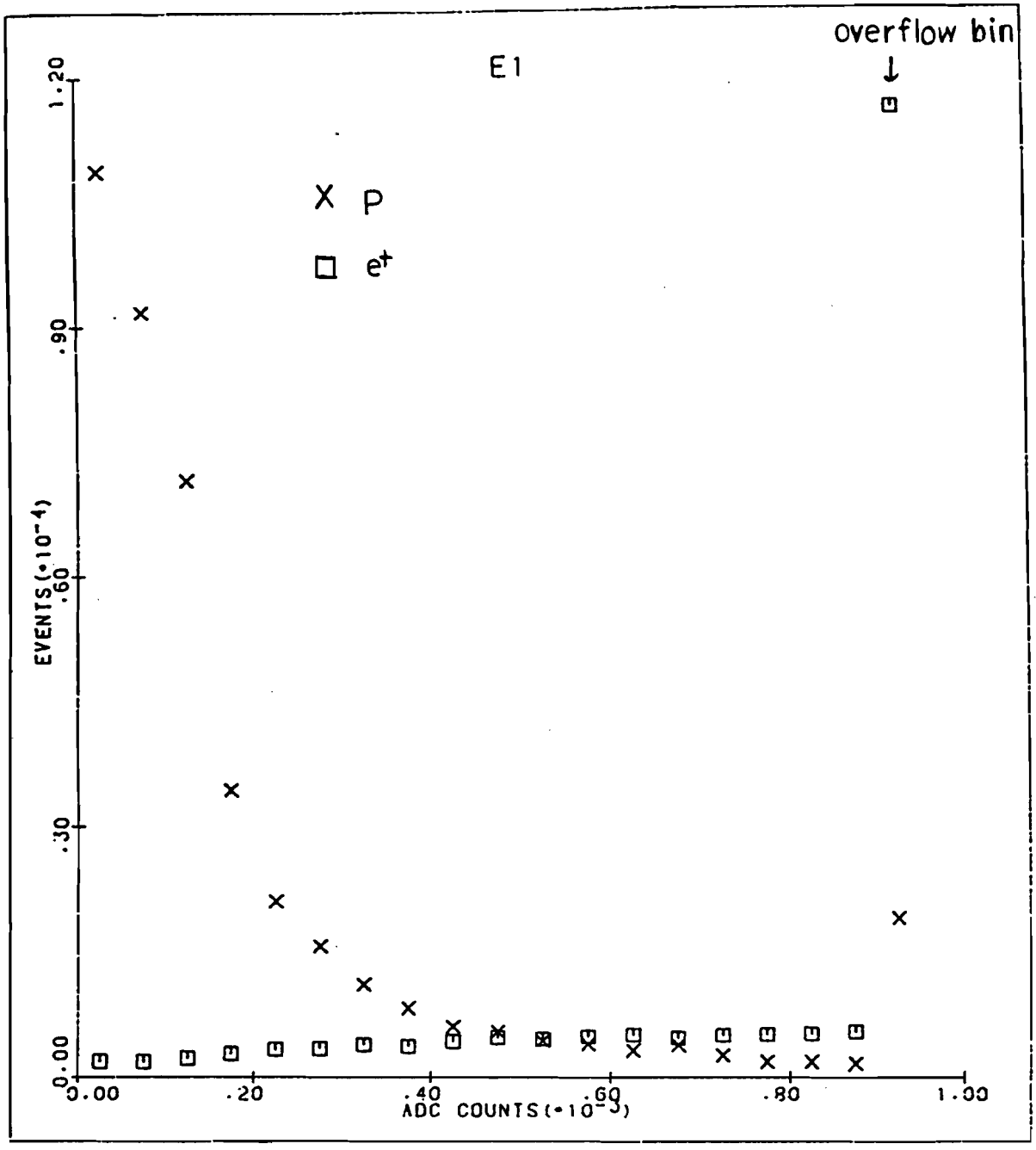

Figure 13. E1 Pulse Height

the V trigger coincidence logic. Offline analysis of the events accumulated in these trigger studies indicated that the logical combination S2•S3 was responsible for an overall non-leptonic lambda decay inefficiency of 10%. Each of the scintillation counters from which these pulses were derived intercepted just one of the charged particles in an event, and the distance from the location of the appropriate charged particle at the counter position to the phototube viewing the counter could be calculated. The inefficiency was a function of these two distances, and was a consequence of relative widths and timing of the pulses used in the coincidence logic. The efficiency of the larger counter S2 as a function of the distance between the phototube and the location of the negatively charged particle at the counter position was also measured, dropping 6% over the length of the counter.

4.6 Solutions in the Lambda Rest Frame

The measurement of the ratio of the coupling constants in lambda beta decay required a calculation of the electron and neutrino directions in the lambda rest frame. The momentum four-vectors of the proton [$P_p = (E_p, \vec{P}_p)$] and electron [$P_e = (E_e, \vec{P}_e)$], measured in the laboratory frame, could be boosted into the lambda rest frame once the

laboratory lambda momentum vector was determined. Unfortunately, the laboratory momentum vector of the lambda in a lambda beta decay candidate could not be unambiguously determined because the neutrino remained undetected. This section discusses the manner in which this problem was handled and how each lambda beta decay was kinematically reconstructed in the lambda rest frame.

The laboratory momentum vector of the lambda was written:

$$\vec{P}_\Lambda = P_\Lambda \hat{\Lambda} ,$$

where $P_\Lambda = (\gamma^2-1)^{1/2} M_\Lambda$ was the unknown momentum magnitude. The unit vector along the lambda direction in the laboratory was denoted by $\hat{\Lambda}$. This unit vector was determined by two sets of coordinates; the measured lambda decay vertex was one, and the point in the production target at which the lambda originated was the other. The lambda was assumed to originate at the center of the target in the x-y plane at the z coordinate of the target. The x and y coordinates for the center of the target in that plane were determined with the prescaled non-leptonic lambda event sample; the extrapolated intercepts of the measured lambda momentum vectors with the target plane were calculated for the non-leptonic events. The mean values

for the resulting x and y distributions at the target plane determined the coordinates for the center of the target.

The only quantity determined unambiguously in the lambda rest frame using the measured laboratory quantities was the neutrino energy

$$\nu = e_m - \frac{1}{M_\Lambda}\left(\underline{p}_e \cdot \underline{p}_p\right) .$$

The c.m. electron and proton energies, respectively denoted e and b, were calculated using the laboratory lambda momentum vector defined above:

$$e = \gamma E_e - (\gamma^2-1)^{1/2}\, \vec{p}_e \cdot \hat{\Lambda}$$

$$b = \gamma E_p - (\gamma^2-1)^{1/2}\, \vec{p}_p \cdot \hat{\Lambda} \quad .$$

Conservation of energy in the lambda rest frame required

$$M - \nu = e+b \quad .$$

The expressions for the c.m. energies were substituted into this equation; subsequent rearrangement yielded a

quadratic equation for γ with two solutions:

$$\gamma_{1,2} = \frac{(M_\Lambda - \nu)E \pm (\vec{p}\cdot\hat{\Lambda})(\nu_L^2)^{1/2}}{E^2 - (\vec{P}\cdot\hat{\Lambda})^2} .$$

where $E = E_e + E_p$ and $\vec{P} = \vec{P}_e + \vec{P}_p \equiv (P_1, P_2, P_3)$.

The discriminant of the quadratic equation was the square of the c.m. neutrino longitudinal momentum

$$\nu_L^2 = \nu^2 - P_T^2 ,$$

where $\vec{P}_T$ was the vector sum of the transverse momenta of the proton and the electron in the laboratory with respect to the lambda direction:

$$\vec{\rho}_T = \vec{p} - (\vec{p}\cdot\hat{\Lambda})\hat{\Lambda} \equiv (t_1, t_2, t_3) .$$

There were two real solutions for γ when $\nu_L^2 > 0$. An event of this type thus had two ambiguous solutions in the lambda rest frame. This condition applied for 68% of the final sample of lambda beta decays described in Section 4.7.

The quadratic equation for γ had a negative discriminant when $\nu_L^2 < 0$. The procedure adopted for these events was to change the lambda direction ($\hat{\Lambda}$) assumed in the original calculations and subsequently force the event to satisfy condition $\nu_L^2 = 0$. An event of this type had a unique solution in the lambda rest frame, because the quadratic equation had two degenerate real solutions for γ. These adjusted events occurred as a result of the limited resolution of the magnetic spectrometer and the lack of knowledge concerning the target position at which the lambda originated.

The adjustment proceeded by fixing the lambda decay vertex coordinates, denoted (x,y,z), and allowing the lambda to originate at a point other than the the center of the production target in the x-y plane at the z coordinate of the target. The point of origin was assumed to lie a radial distance D from the center of the production target in a direction opposite to the projection of $\vec{P}_T$ in the target plane. This resulted in a quadratic equation for D:

$$aD^2 + bD + c = 0 \quad .$$

The smaller of the two solutions for D, denoted D_o, was then used to adjust ν_L^2 . Background in the adjusted event component of the lambda beta decay sample could be removed by requiring the parameter D_o^2 to lie below 15 mm^2.

The coefficients in the equation could be expressed in terms of the following definitions:

$$k_i = P^2 - \nu^2 - P_i^2 \quad (i = 1,3)$$

$$(u,v) = -(\cos\phi, \sin\phi)$$

$$\phi = \tan^{-1}(t_2/t_1).$$

The coefficients were then calculated to be:

$$a = k_1 u^2 + k_2 v^2 - P_1 P_2 uv$$

$$b = P_3 z(P_1 u + P_2 v) + P_2 y P_1 u + P_1 x P_2 v - 2k_1 ux - 2k_2 vy$$

$$c = k_1 x^2 + k_2 y^2 + k_3 z^2 - P_1 P_2 x y - P_3 z (P_1 x + P_2 y).$$

4.7 The Final Data Sample

The final sample of lambda beta decays was chosen with electron signature requirements from the lead glass and synchrotron radiation detectors corresponding to respective lambda beta decay efficiencies of 96% and 71%. The overall non-leptonic lambda rejection of this combination was a factor of 10^4. Other demands imposed on the final data sample included a fiducial cut on the proton position at S3 and a requirement that the ratio of the momentum of the positively charged particle to the negatively charged particle in the laboratory was larger than the minimum

value for a lambda beta decay, which was 2.4. The adjusted events were required to have $D_o^2 < 15mm^2$. Finally, a hadronic signature from E1 required that less than 800 counts had been recorded by the appropriate ADC channel.

There were 92,302 events remaining after these requirements were applied to the reconstructed lambda beta decay triggers. The p-pi invariant mass distribution is presented for these events in Figure 14.

A reduction in the remaining non-leptonic lambda decay background, which accounted for 25% of the events, could be accomplished through the application of successively more stringent offline electron signature requirements from the lead glass and synchrotron radiation detectors. The efficiencies of two tighter electron signatures have been presented for each detector in Sections 4.2 and 4.3. The effect of combining the first set of tighter requirements from both detectors is shown in Figure 15. The tightest electron requirements discussed for the detectors result in the invariant mass distribution shown in the subsequent plot. In each case, the number of events (N_T) and the product of the electron efficiencies from the independent detectors (ϵ_β) are noted.

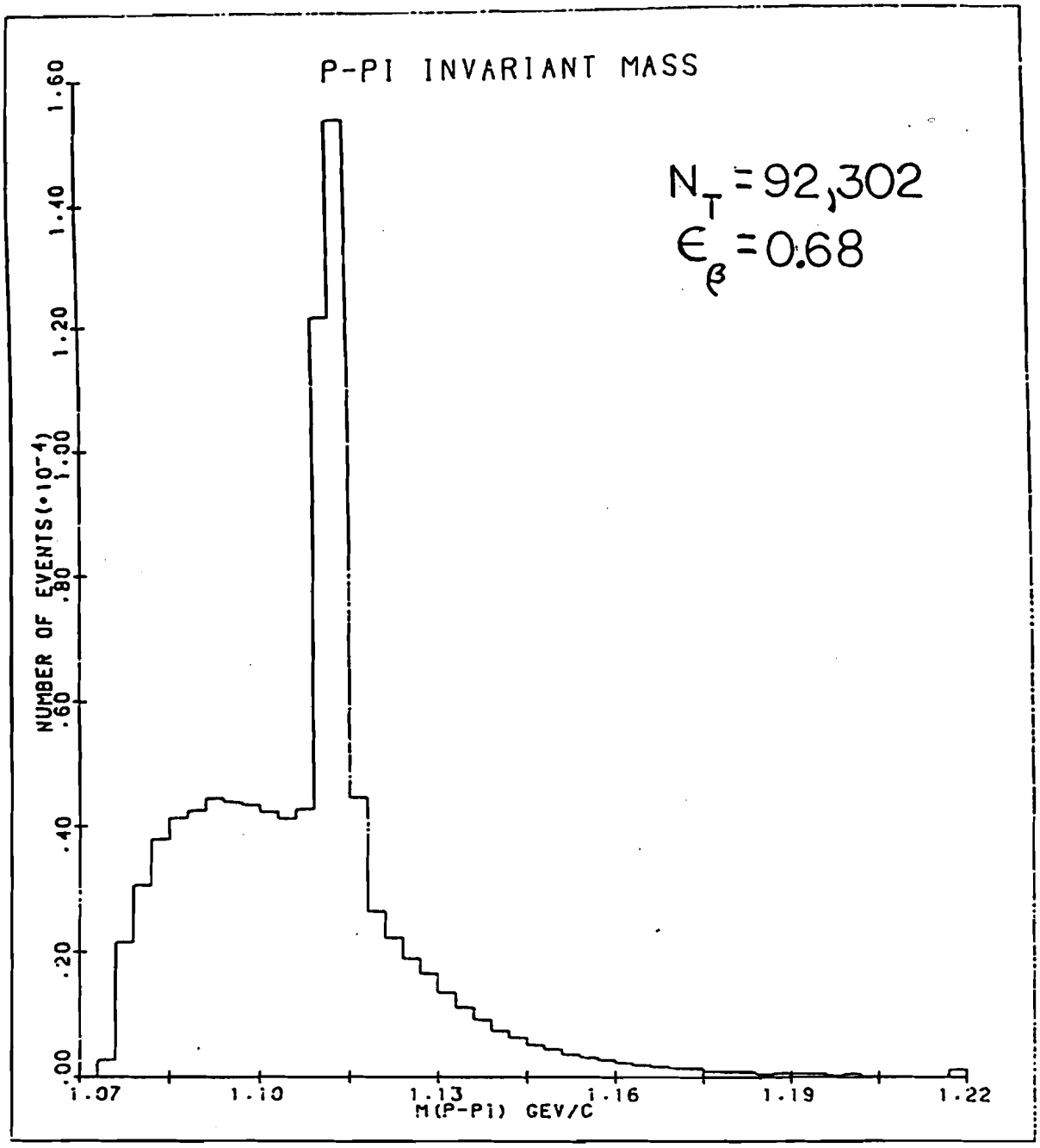

Figure 14. P-Pi Invariant Mass - Final Sample Before Mass Cut

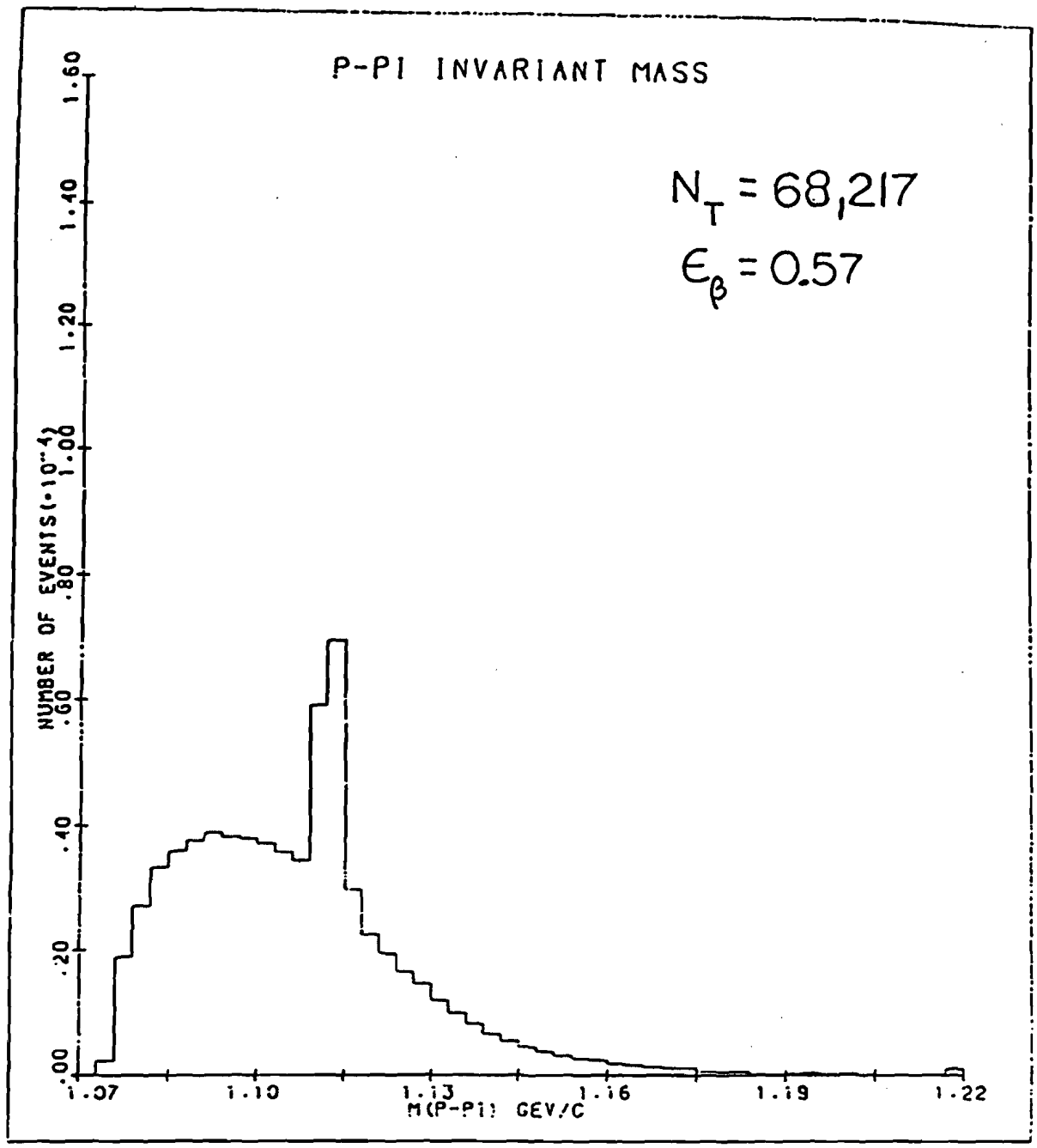

Figure 15. P-Pi Invariant Mass - Tighter Electron Requirements

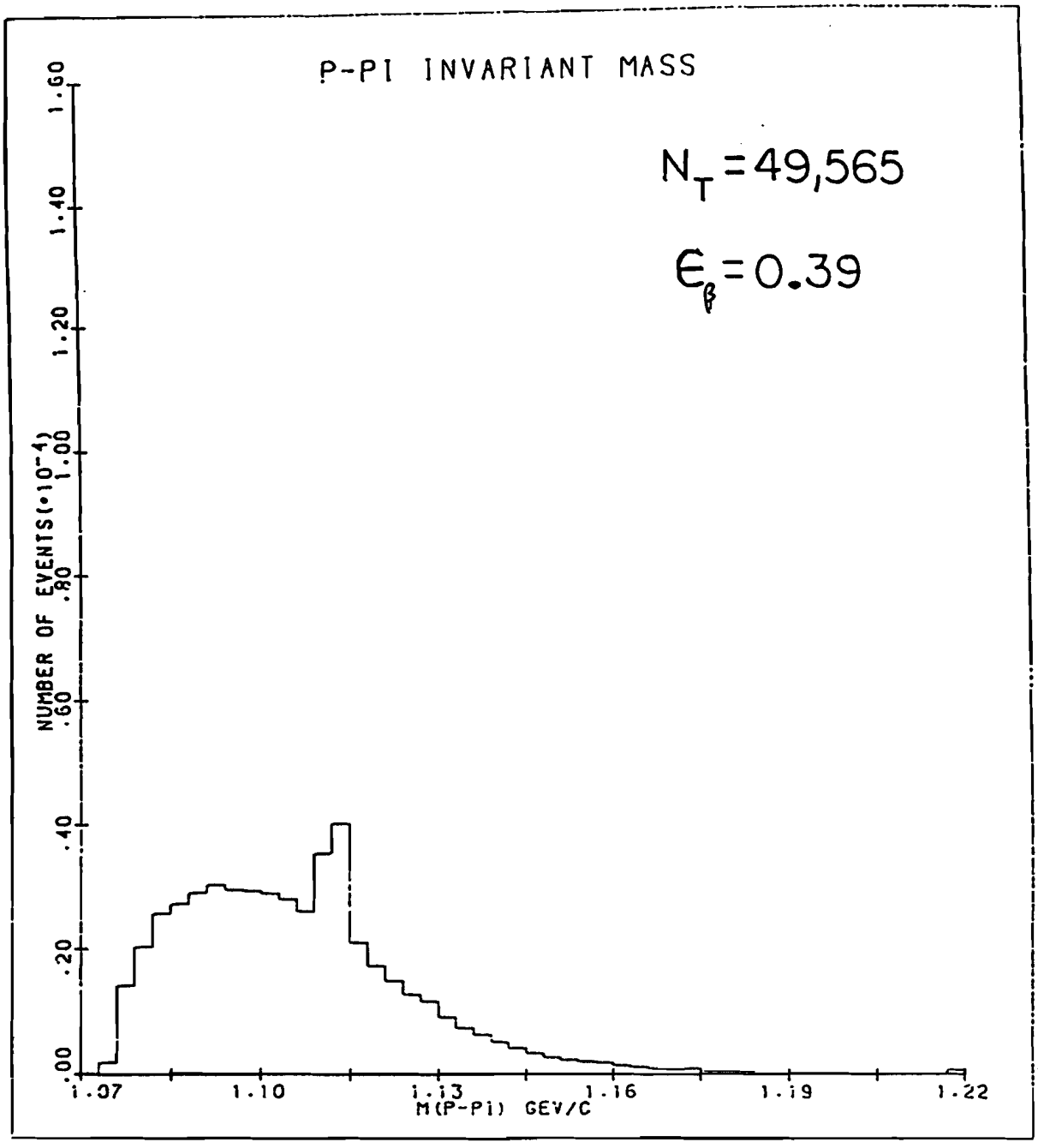

Figure 16. P-Pi Invariant Mass - Tighter Electron Requirements

Another way to remove the non-leptonic lambda decay background in the data sample shown in Figure 14 was to cut any event fitting the non-leptonic $\Lambda \rightarrow p\pi^-$, $K^0_S \rightarrow \pi^+\pi^-$ and $\bar{\Lambda} \rightarrow \bar{p}\pi^+$ decay hypotheses. There were 55,752 events in the final sample of lambda beta decays after this mass cut was imposed. This is the sample to which the analysis described in the next chapter applies.

The advantage of such a mass cut was that an understanding of the systematic effects in the determination of the electron identification efficiency was maintained. The Monte Carlo studies discussed in the next chapter indicated that only 21% of the lambda beta decays had been removed with such a mass cut, and that the residual non-leptonic lambda decay background in the sample was less than 1%.

CHAPTER 5

ANALYSIS AND RESULTS

5.1 The Monte Carlo Simulation

It was necessary to correct the experimental data for the combined acceptance of both the apparatus and the offline software requirements. This was accomplished with a Monte Carlo simulation of the experiment. The Monte Carlo generated neutral strange particles at the production target and propagated them through the defining hole in the collimator. Decays via charged modes were allowed to occur in the decay region with spatial distributions consistent with the known particle lifetimes. The kinematics for such non-leptonic two body decay processes as $\Lambda \rightarrow p\pi^-$ and $K^0_S \rightarrow \pi^+\pi^-$ were trivial because the decay products have a

unique momentum in the parent rest frame. The three body semi-leptonic decays were encoded by assuming a form for the square of the matrix element in order to simulate the correct Dalitz plot density. The lambda beta decay distribution will be discussed in Section 5.2.1. The Ke3 decays were generated using the conventions and parameters published by the Particle Data Group [2].

The momentum four-vectors of the decay products in the laboratory frame were obtained by applying a Lorentz transformation to the momentum four-vectors of the decay products generated in the parent rest frame. The charged decay products were permitted to propagate through the apertures of the magnetic spectrometer and were deflected in the magnetic field of the analyzing magnet. Multiple Coulomb scattering occurred in the material before every MWPC and the charged pions were allowed to decay in flight. An adjustment of the laboratory electron energy, resulting from bremsstrahlung in the material upstream of the analyzing magnet, was also performed for the semi-leptonic events. The V trigger requirements were applied to the charged particles; the counter geometry and efficiencies were included for all events. The semi-leptonic events were affected by the measured position and momentum dependent efficiencies of the synchrotron radiation and lead glass detectors, as well as the threshold Cerenkov counter trigger efficiency for protons and pions.

The positions of the charged particles at the MWPC sense planes were converted into wire numbers corresponding to the real MWPC wire positions. Chamber inefficiences, adjacent multiple hits and accidental wire hits were included in the simulation. The wire hits were used by the same software that handled the real data to reconstruct the neutral vee topology. The analysis of the reconstructed Monte Carlo events proceeded in a fashion identical with the treatment of the real data.

5.1.1 Acceptance and Backgrounds

The spectrometer acceptance for lambda beta decays occurring in the decay region is shown in Figure 17. This included the effects of the geometrical acceptance, the V trigger efficiency, the reconstruction efficiency and the offline fiducial cuts. The corresponding acceptance for non-leptonic lambda decays occurring in the decay region is also plotted in Figure 17 for comparison.

The relative acceptance of the final lambda beta decay sample as a function of the position on the Dalitz plot is presented in Figure 18. This included both the particle identification criteria and kinematic requirements used in defining the final lambda beta decay sample, which are

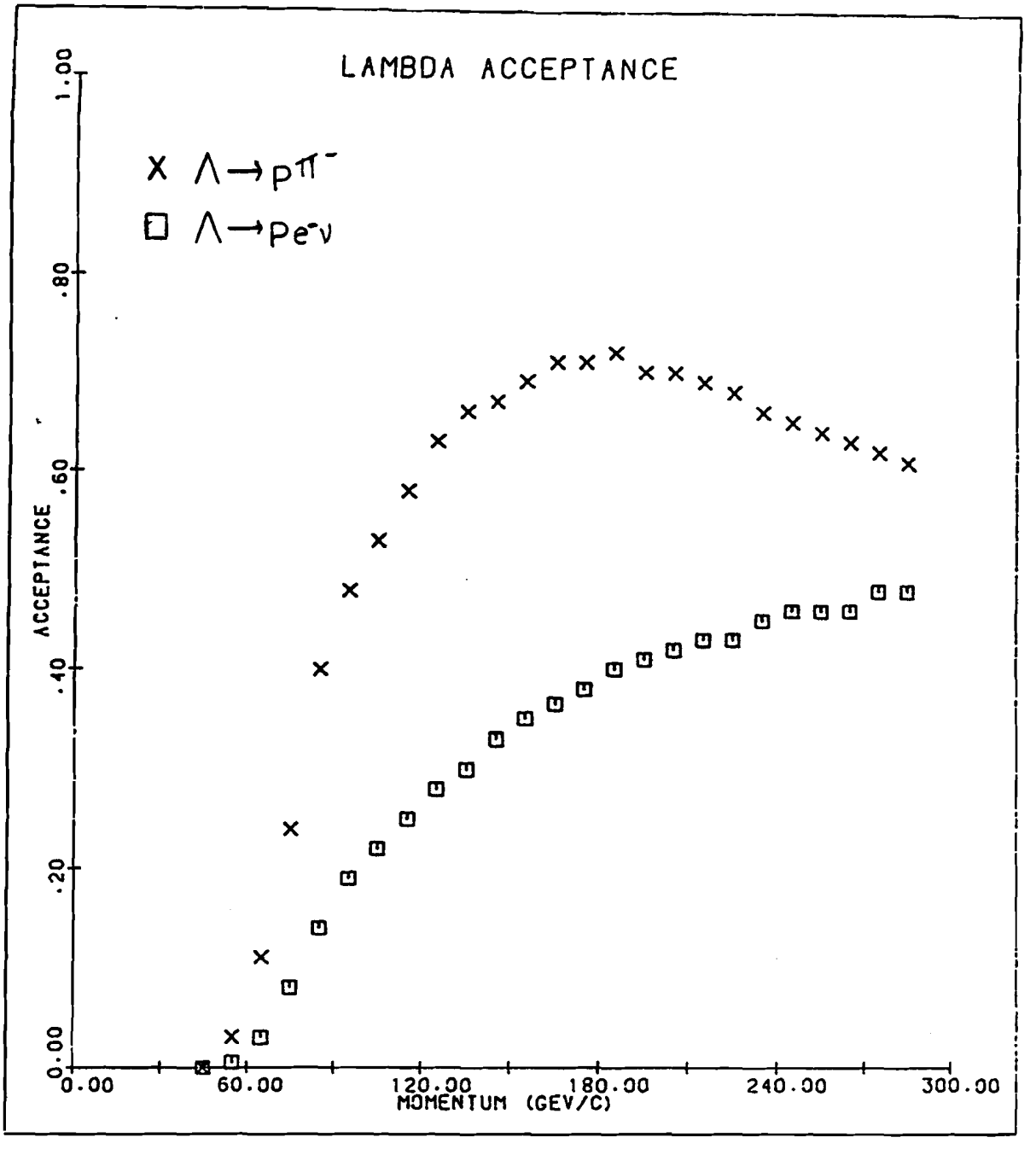

Figure 17. Lambda Acceptance

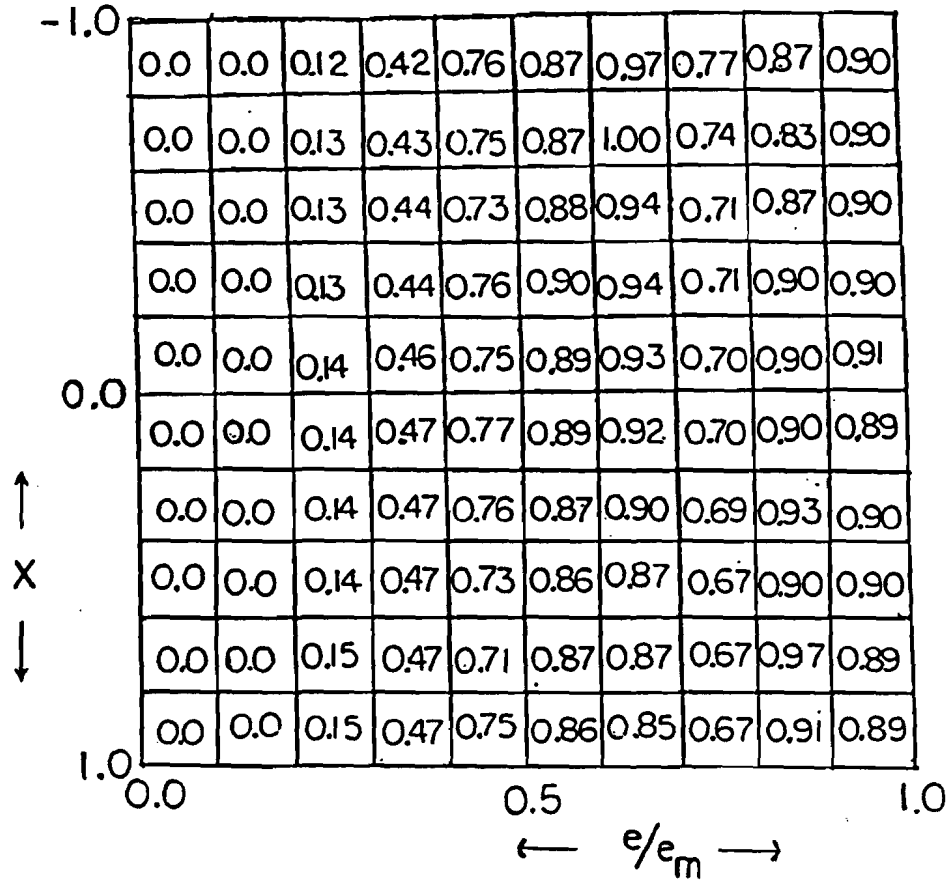

Figure 18. Relative Dalitz Plot Acceptance

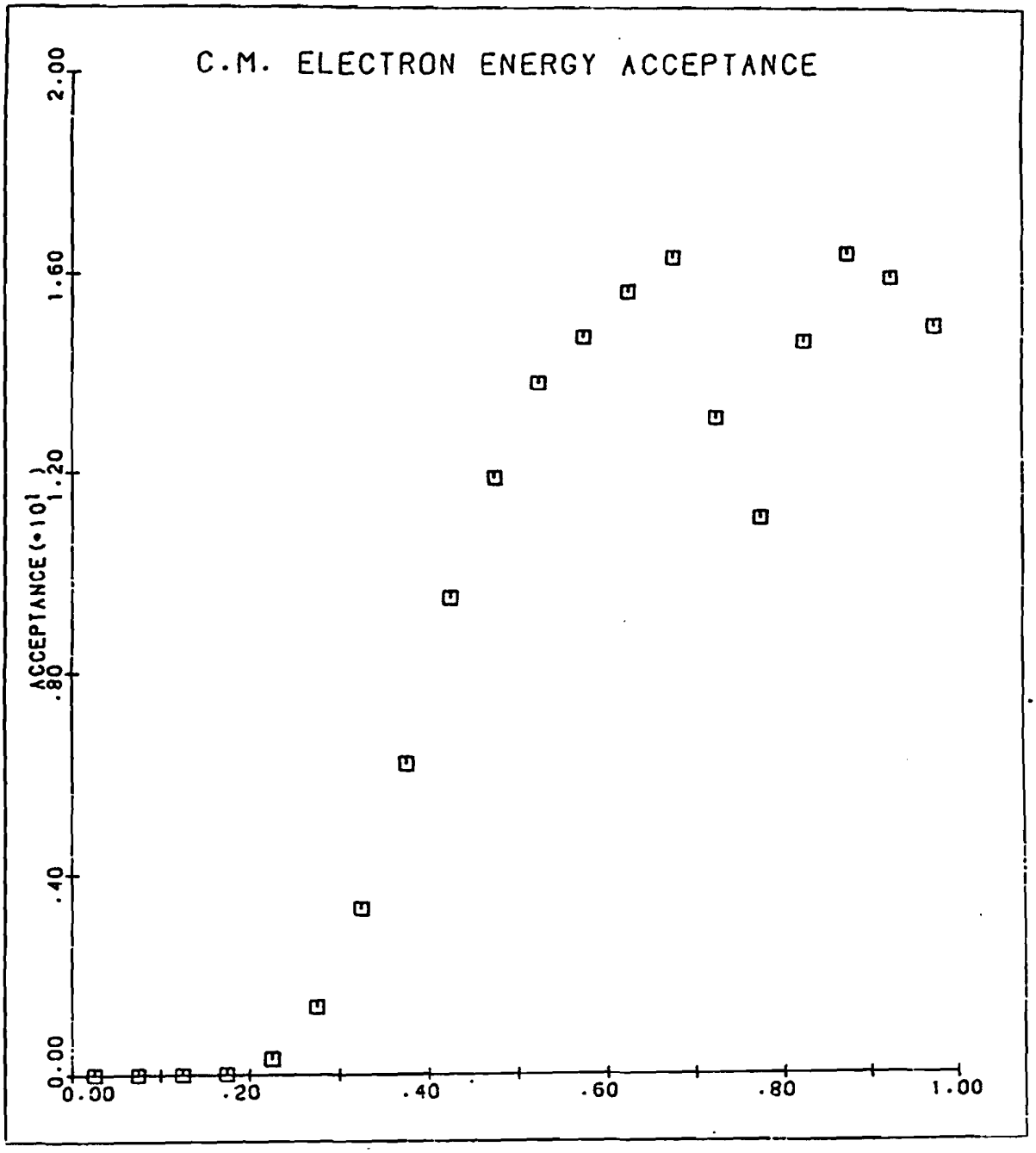

Figure 19. C.M. Electron Energy Acceptance

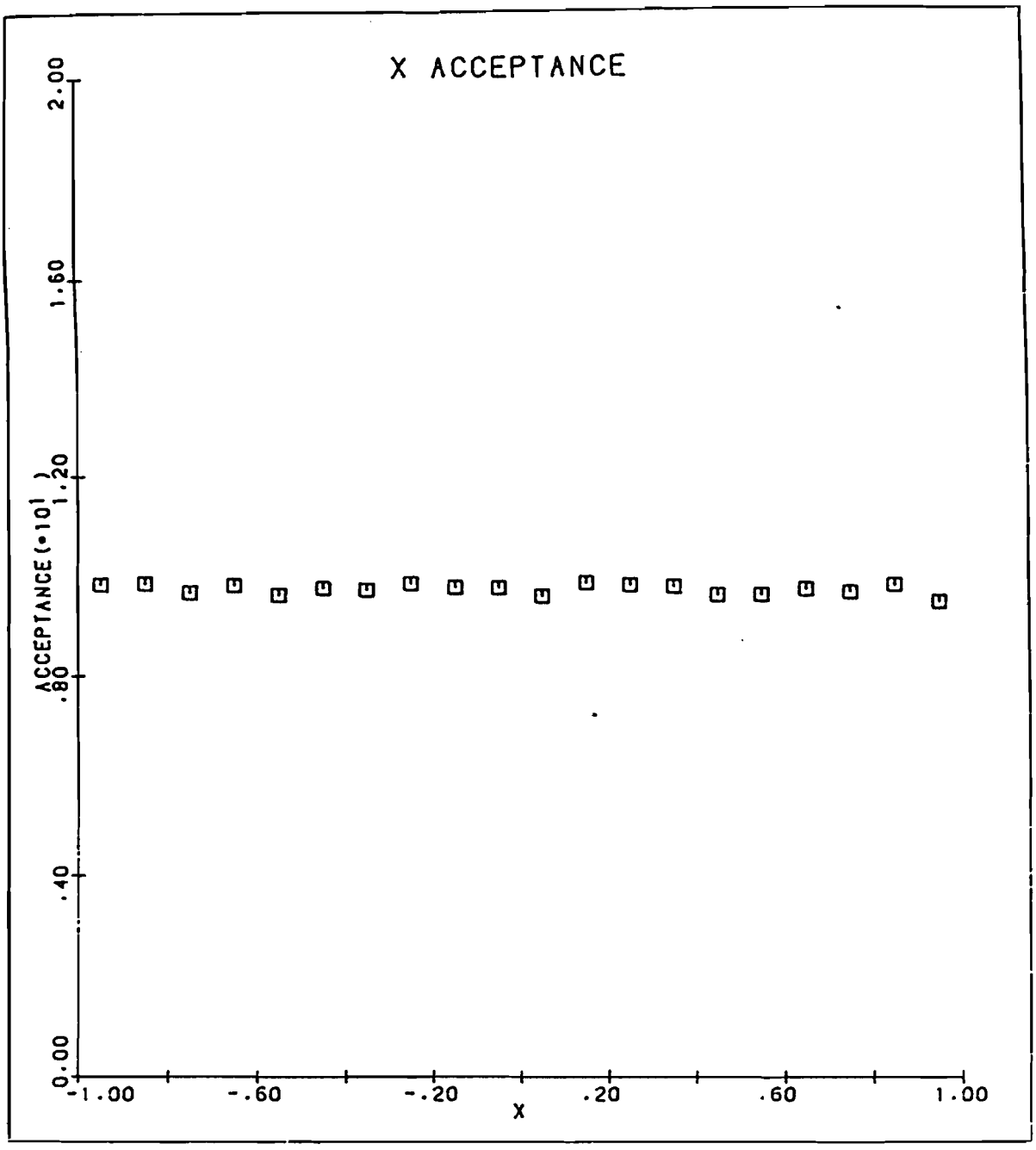

Figure 20. x Acceptance

described in the preceding chapter. The projections of the absolute value of the acceptance along the axes of the Dalitz plot are shown in Figures 19 and 20. The variables corresponding to the two axes are discussed in Chapter 1; e is the c.m. electron energy and x is the cosine of the angle between the neutrino and electron directions in the lambda rest frame.

The estimate of the Ke3 background in the final lambda beta decay sample was obtained by using the Monte Carlo to calculate the overall acceptance for Ke3 decays relative to lambda beta decays for each bin of the lambda momentum spectrum. The Monte Carlo indicated the mean value of the momentum spectrum was at 112 GeV/c. The relative acceptance for decays occurring in the decay region, including the supression provided by the threshold Cerenkov counter and the kinematic requirements described in Section 4.7, was 4×10^{-3} at this mean momentum value. Suppression was also provided by the design of the neutral hyperon beam itself. A much smaller percentage of the K_L^o's produced at the target decayed in the decay region as a consequence of the fact that the lifetime of the K_L^o is almost a factor of 200 longer than the lambda lifetime. The background calculation also accounted for the production ratio of K_L^o mesons to lambda hyperons at the production target, which had been measured previously in

the neutral hyperon beam [7]. These contributed suppression factors of resectively 70 and 1.5 at 112 GeV/c, resulting in an estimate of 1.5% for the Ke3 contamination at this mean momentum value. The suppression resulting from the ratios of the K_L^0 to lambda lifetimes and production rates was less effective at lower momentum. The overall Ke3 contamination was estimated to be 2% after integrating over the entire lambda momentum spectrum.

The Monte Carlo indicated that the mass cut described in Section 4.7 removed 97% of the residual non-leptonic lambda decay background in the p-pi invariant mass plot shown in Figure 14. The corresponding efficiency for retaining lambda beta decays was 79%.

5.1.2 Comparisons with the Prescaled Data Sample

The free parameters in the Monte Carlo were chosen to insure that the simulation of the prescaled non-leptonic lambda decay sample was adequate. Comparisons between the experimental data and the Monte Carlo are presented in Figures 21-24.

The invariant mass and the momentum vector of the decaying lambda were calculated using the equations

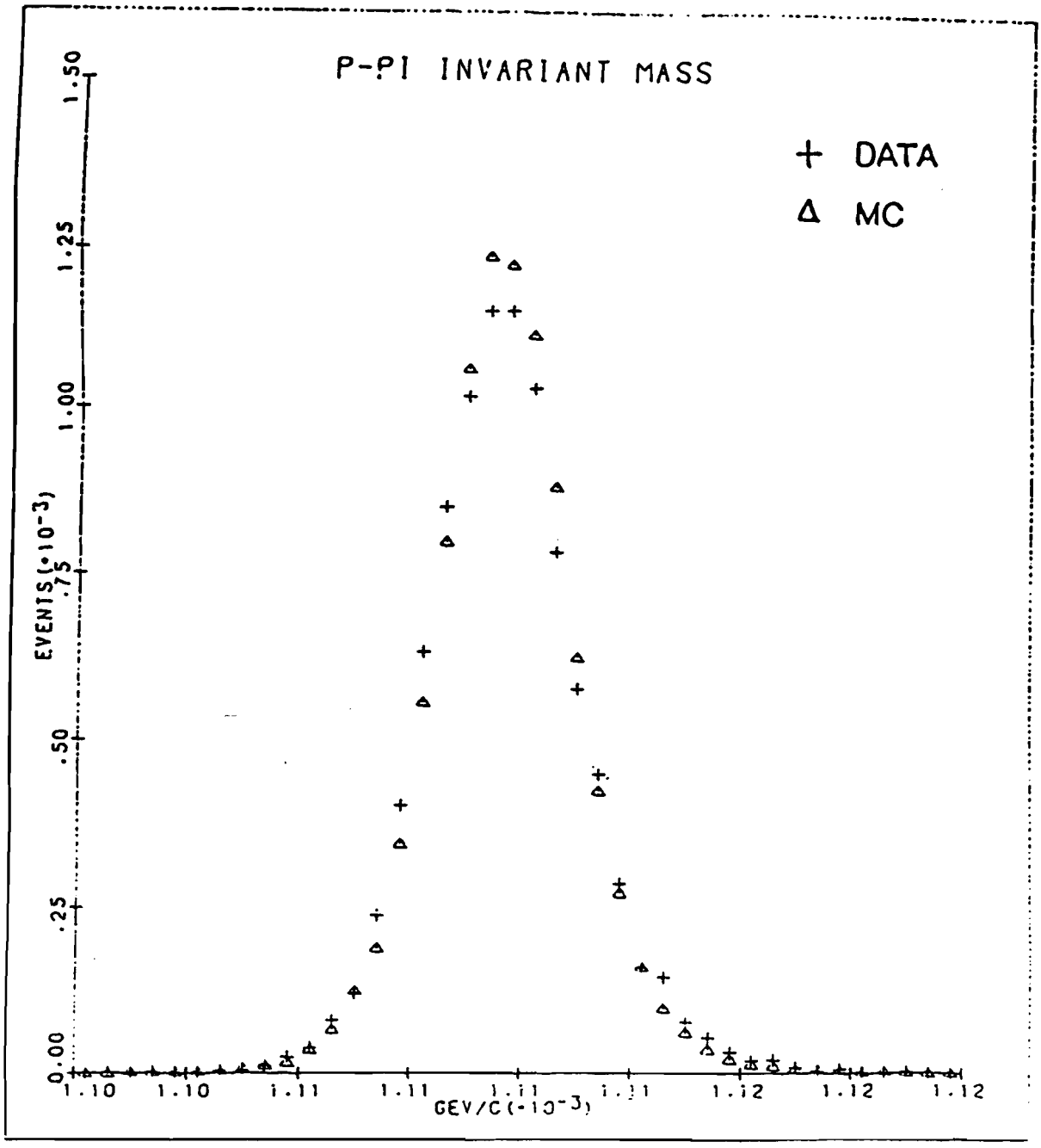

Figure 21. P-Pi Invariant Mass - Non-Leptonic Sample

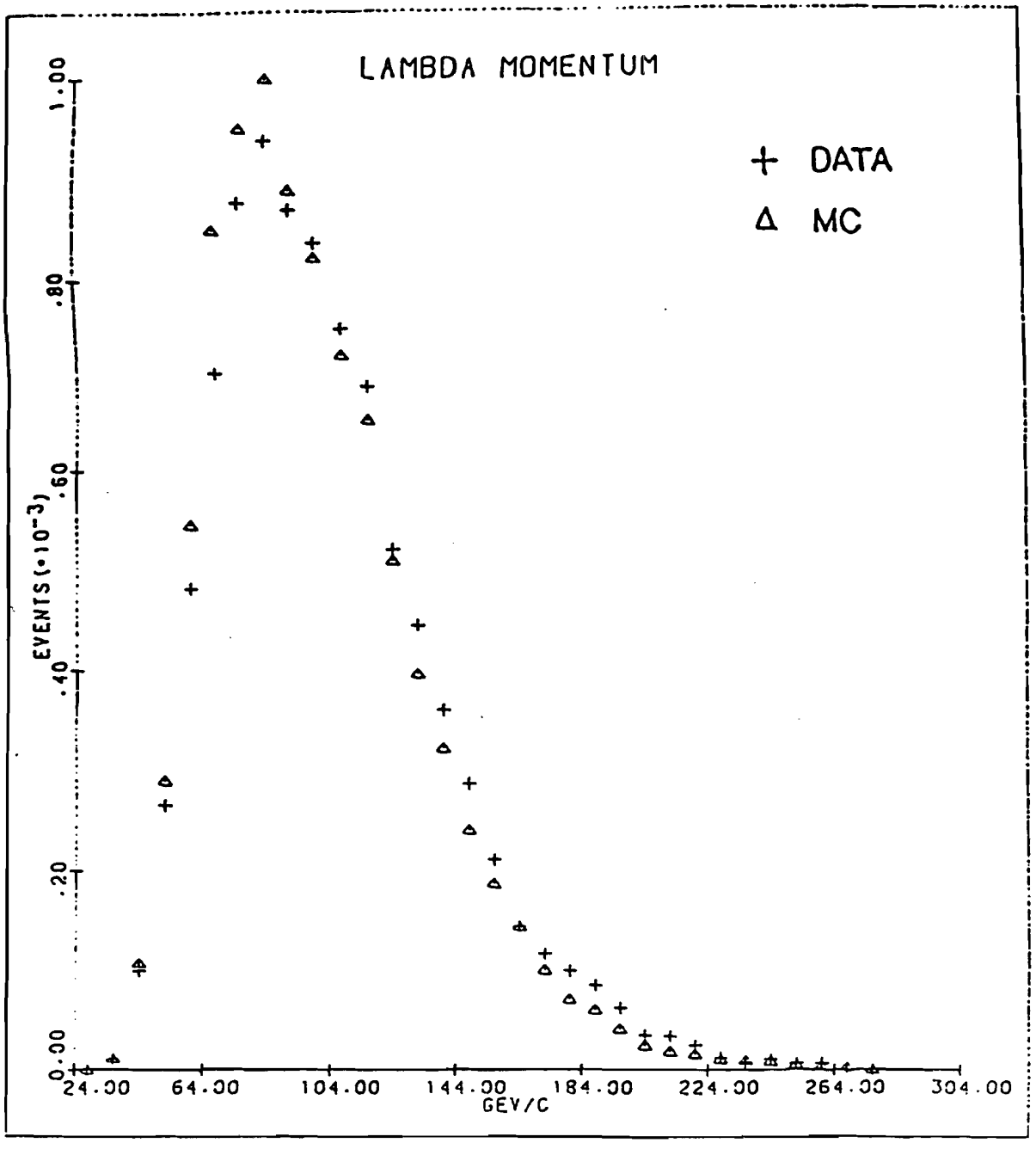

Figure 22. Lambda Momentum - Non-Leptonic Sample

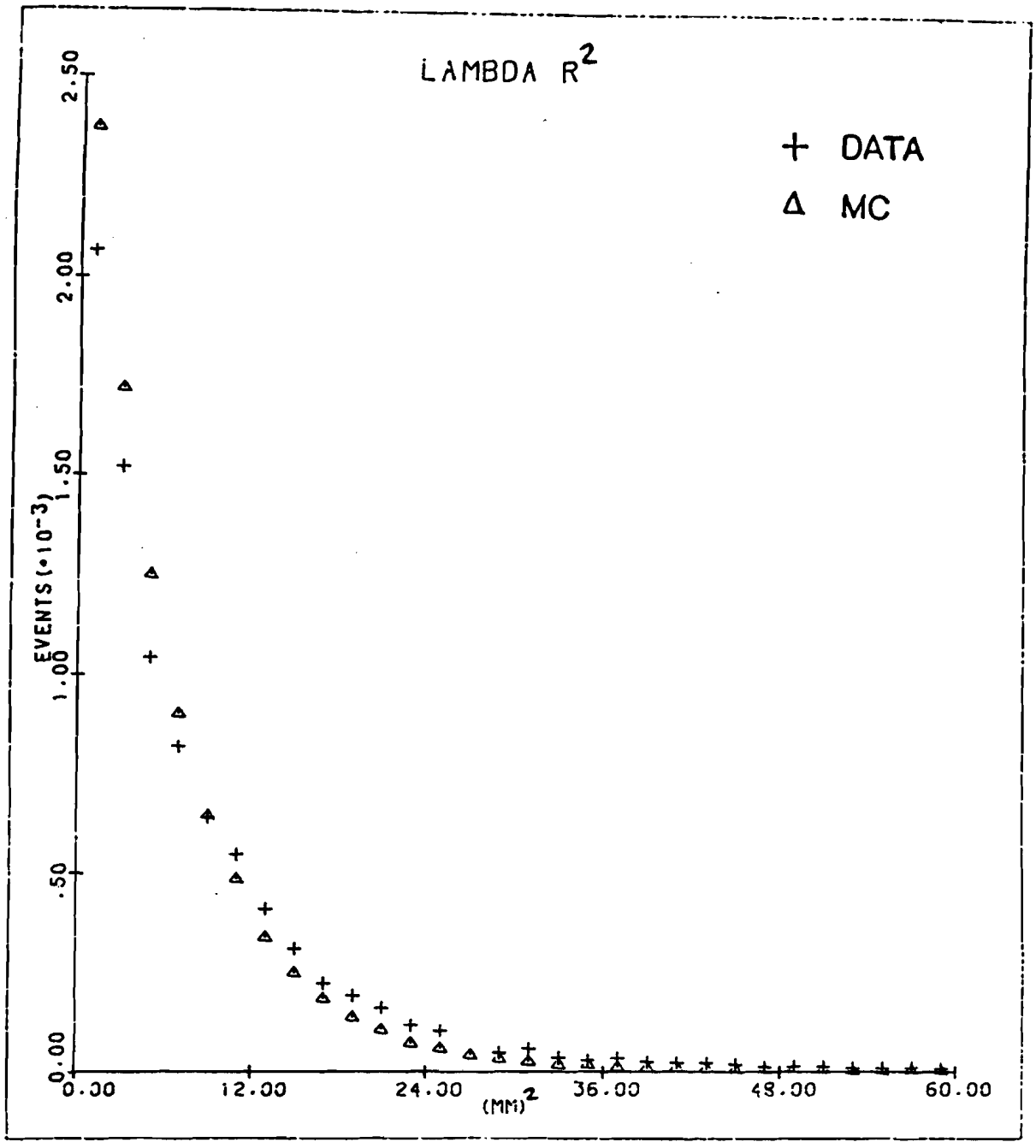

Figure 23. R^2 Distribution - Non-Leptonic Sample

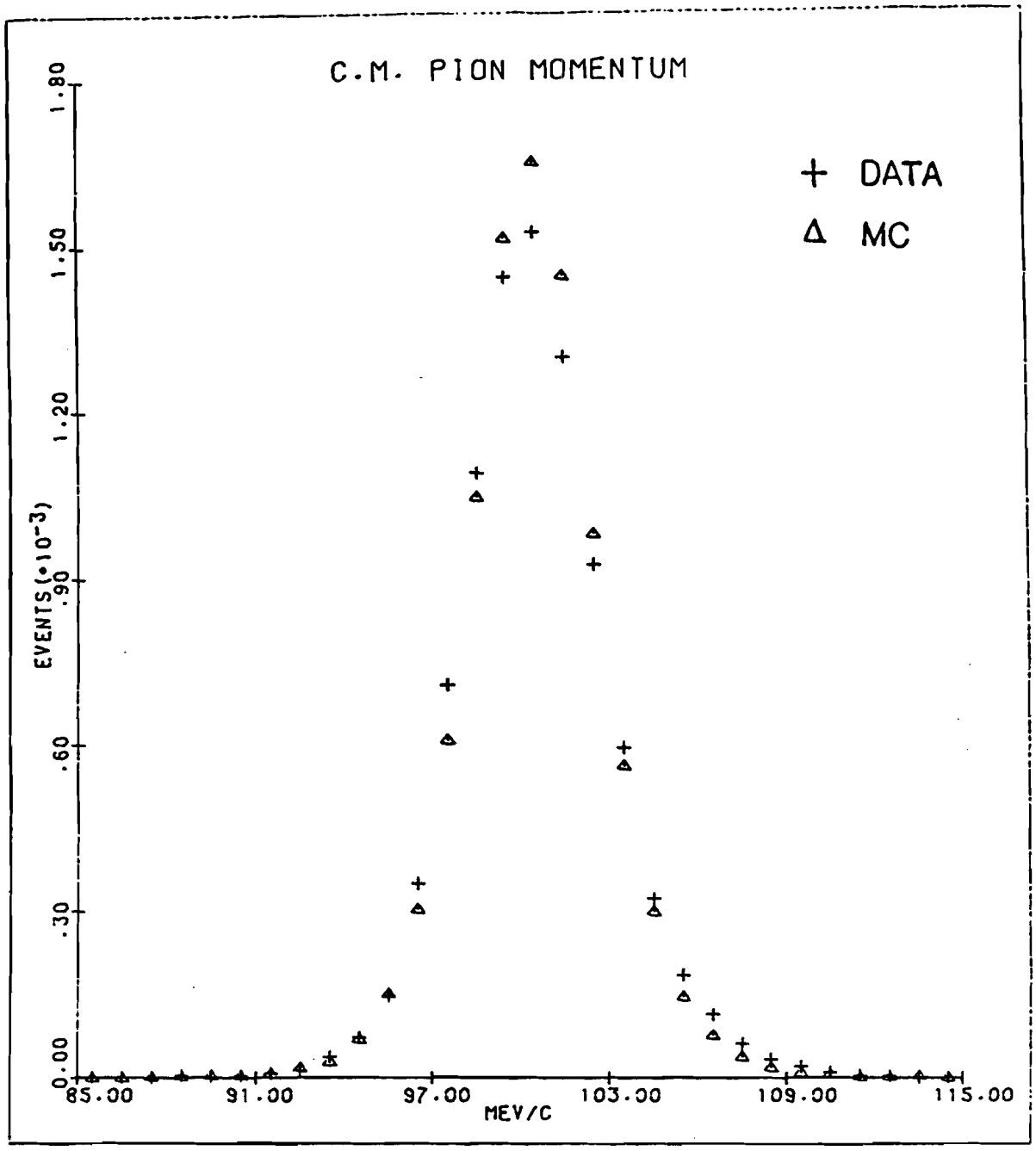

Figure 24. C.M. Pion Momentum - Non-Leptonic Sample

presented in Section 2.2. The p-pi invariant mass distribution was sensitive to the experimental resolution. The lambda momentum spectrum was sensitive to the parent momentum distribution generated at the production target. These are presented in Figures 21 and 22.

The lambda momentum vector was extrapolated back to the x-y plane at the z coordinate of the production target and the radial distance R to the center of the target was then calculated. The lambda R^2 distribution is shown in Figure 23. The tail in the R^2 distribution was the result of two sources of lambda hyperons other than the proton-nucleus collisions in the production target. These were both included in the Monte Carlo simulation. The first was the scattering of the neutral beam in the walls of the defining collimator, which accounted for 5% of the total lambda sample. This contribution was primarily at the lower values of the lambda momentum spectrum. The second was the production of neutral cascade hyperons in the target and their subsequent non-leptonic decay sequence $\Xi^0 \rightarrow \Lambda \pi^0$. The daughter lambda from such a decay acquired an extra transverse momentum which made it unlikely to point back to the center of the target. These daughter lambda's comprised 2.5% of the total lambda component of the neutral beam. A cut on $R^2 > 40$ mm^2 would remove almost 90% of the daughter lambda contribution and

50% of the collimator contribution to the total non-leptonic lambda decay sample accumulated with the V trigger.

The pion momentum in the lambda rest frame was obtained with a Lorentz transformation along the lambda direction measured in the laboratory. The c.m. pion momentum distribution presented in Figure 24 illustrates the effect of the experimental resolution in the lambda rest frame.

5.1.3 Comparisons with the Lambda Beta Decay Sample

Comparisions between the final lambda beta decay sample and the corresponding Monte Carlo simulation are presented in Figures 25-31.

The measured laboratory proton and electron momentum spectra were sensitive to the V trigger efficiency as well as both the online and offline particle identification criteria used in the event selection.

The p-pi invariant mass plot shows the effect of the mass cut on the lambda beta decay sample.

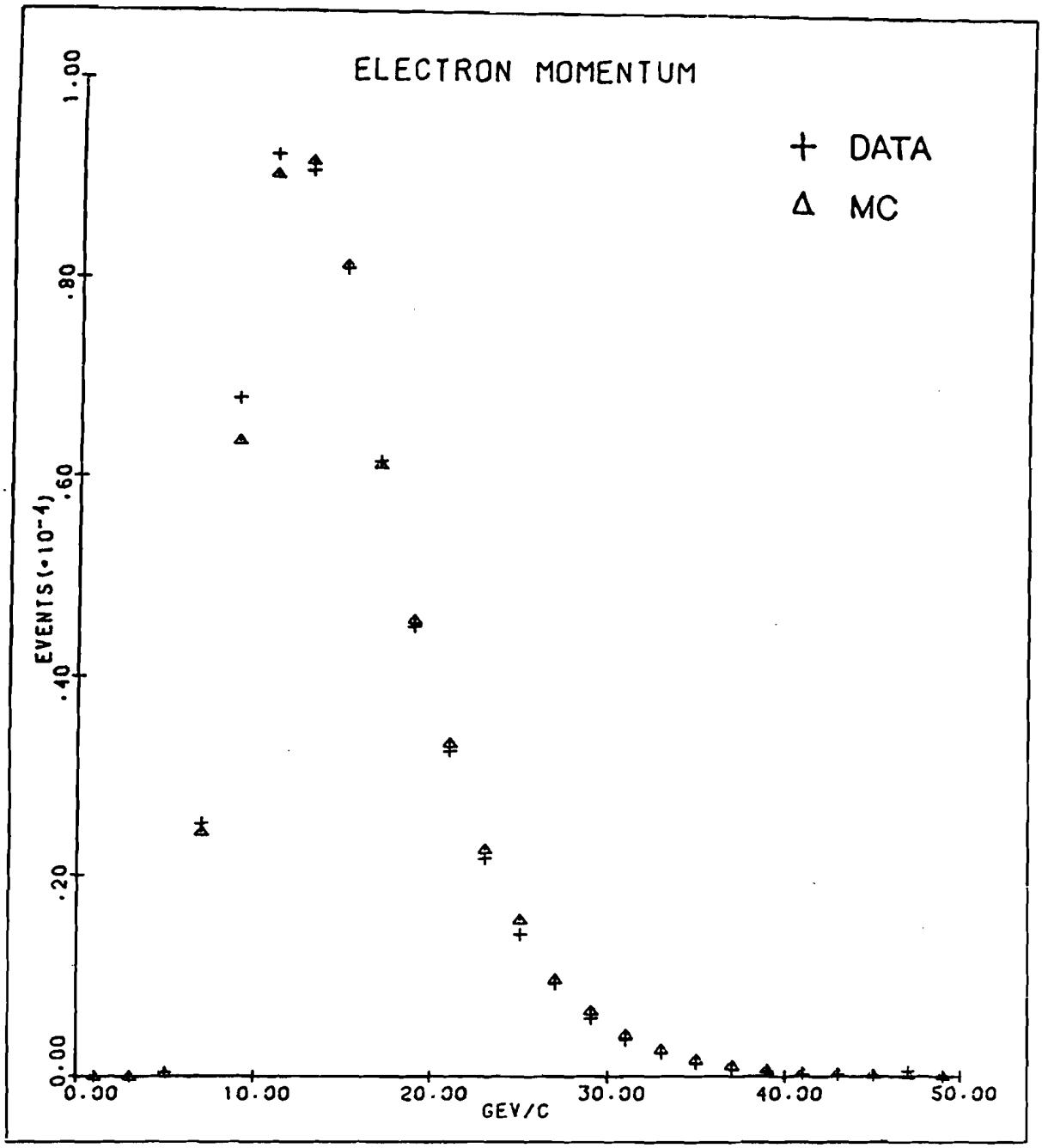

Figure 25. Laboratory Electron Momentum for Lambda Beta Decays

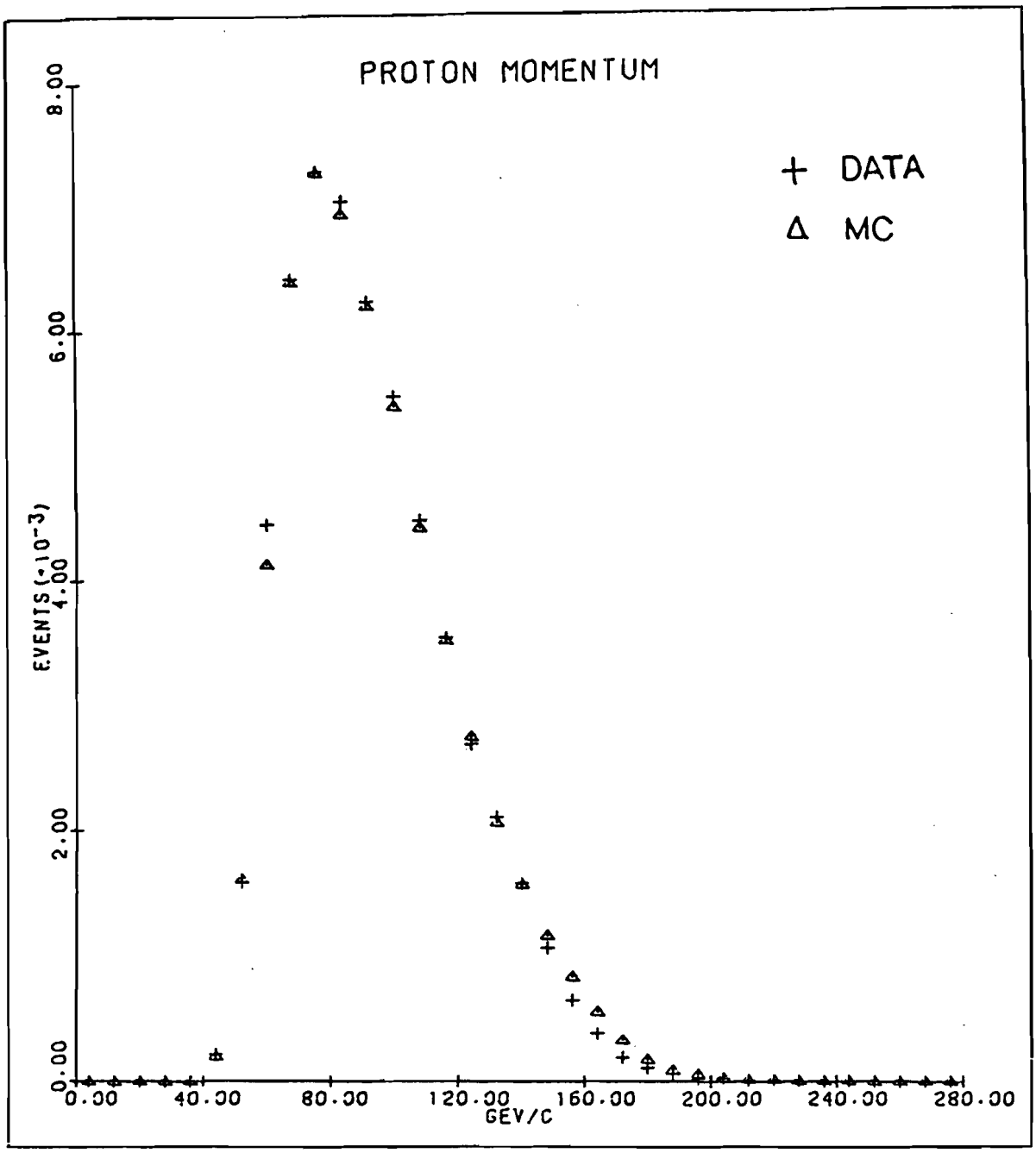

Figure 26. Laboratory Proton Momentum for Lambda Beta Decays

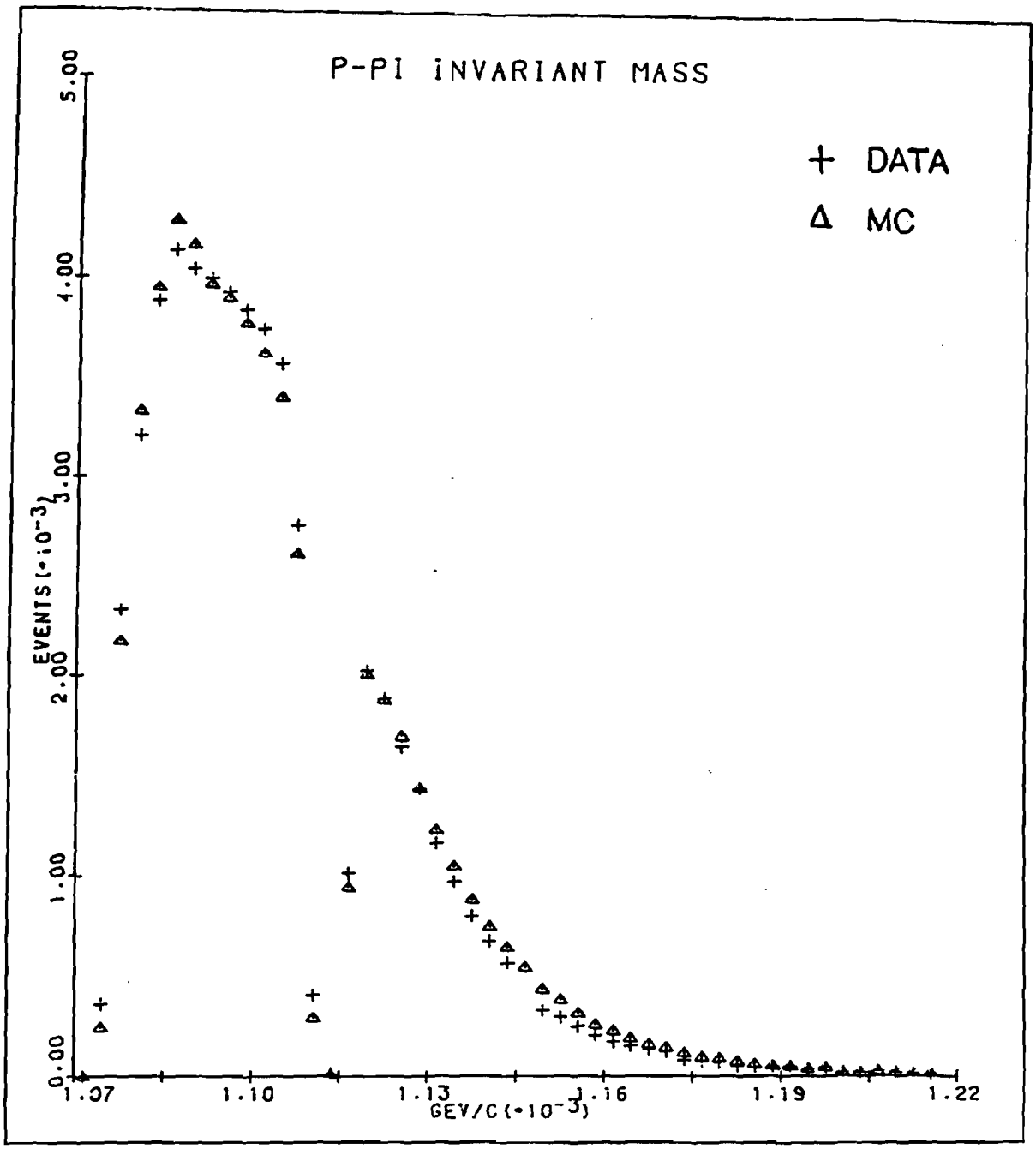

Figure 27. P-Pi Invariant Mass - Lambda Beta Decays

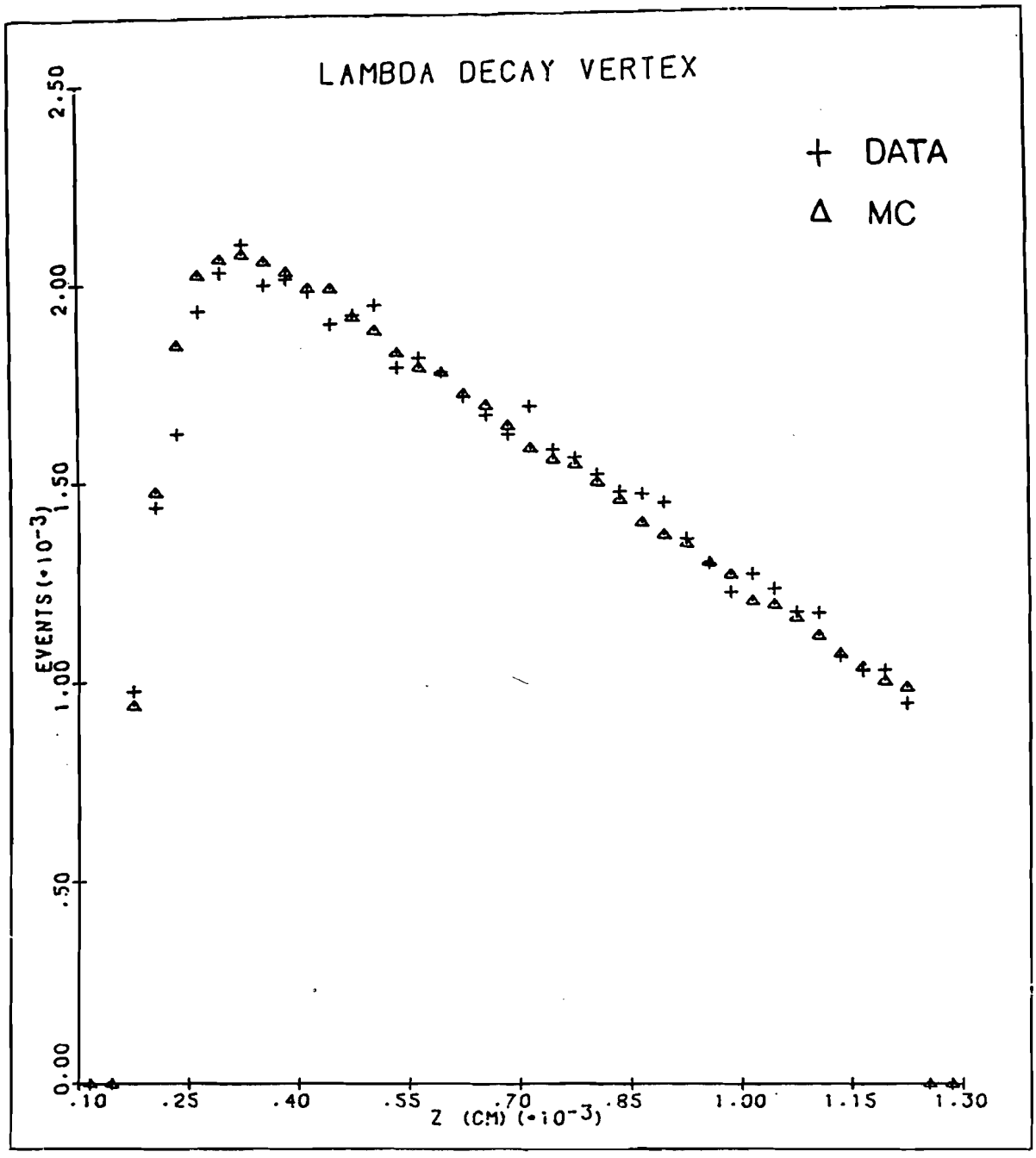

Figure 28. Decay Vertex Distribution - Lambda Beta Decays

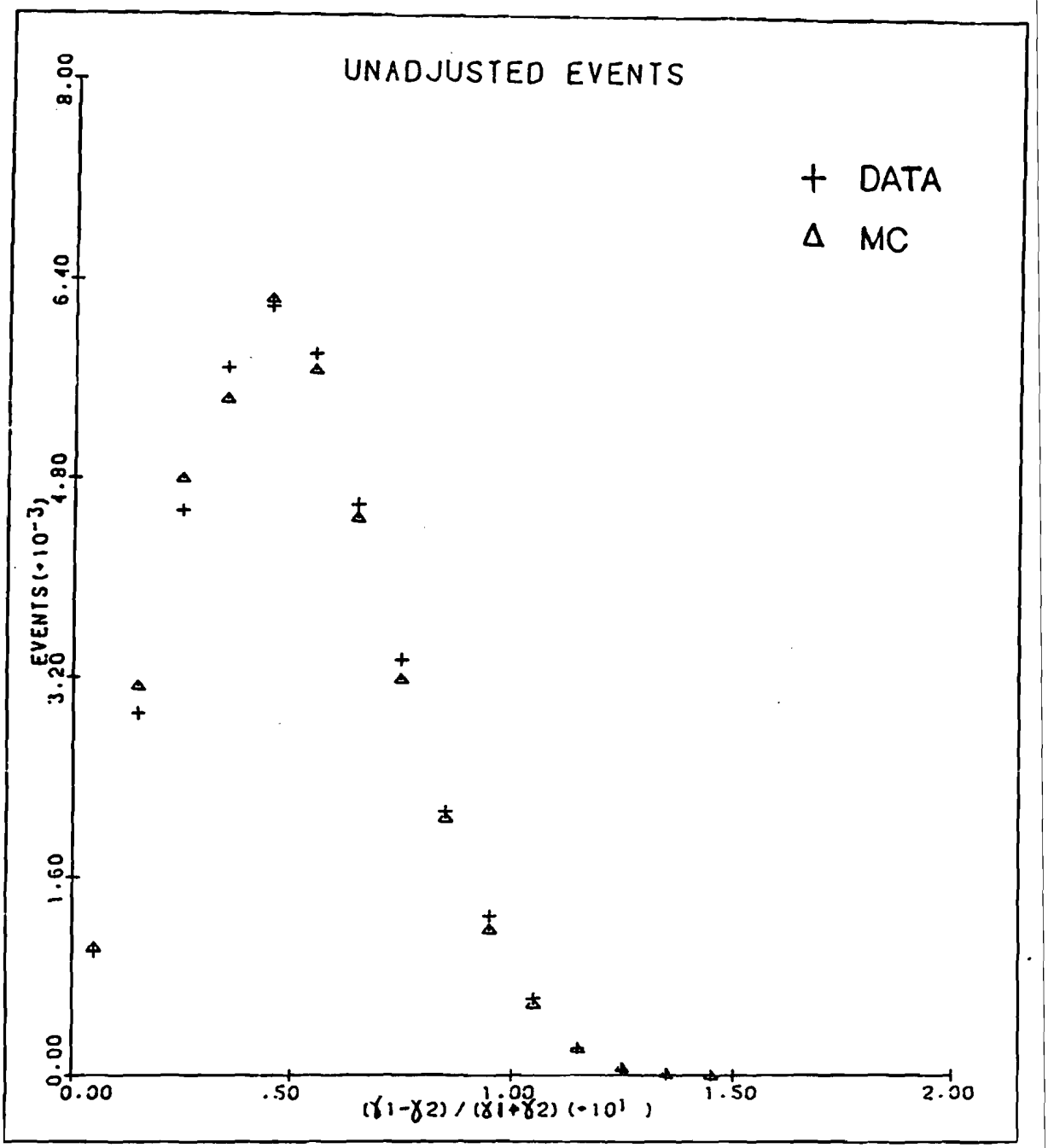

Figure 29. Lambda Momenta Difference - Unadjusted Events

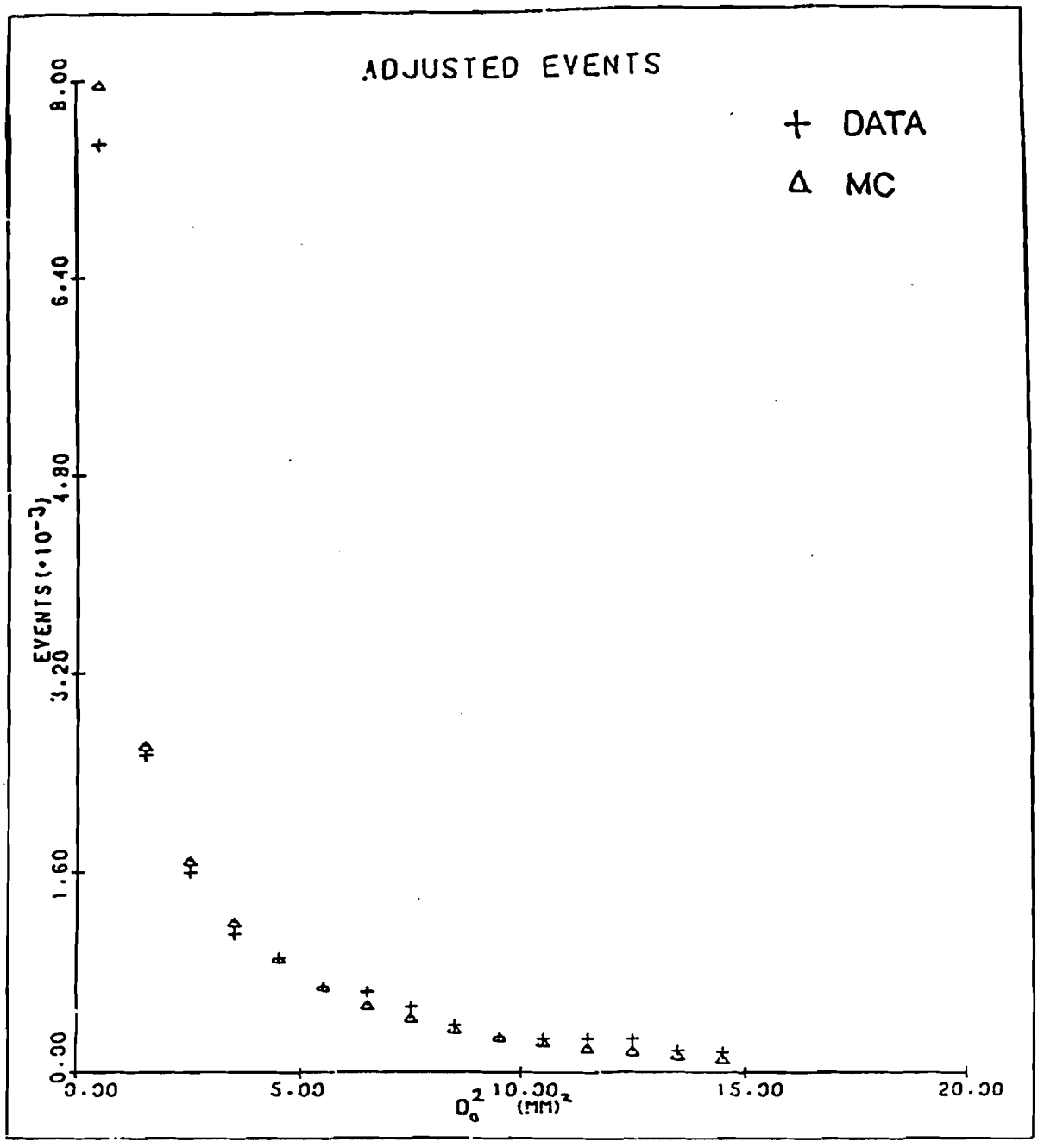

Figure 30. D_o^2 Distribution - Adjusted Events

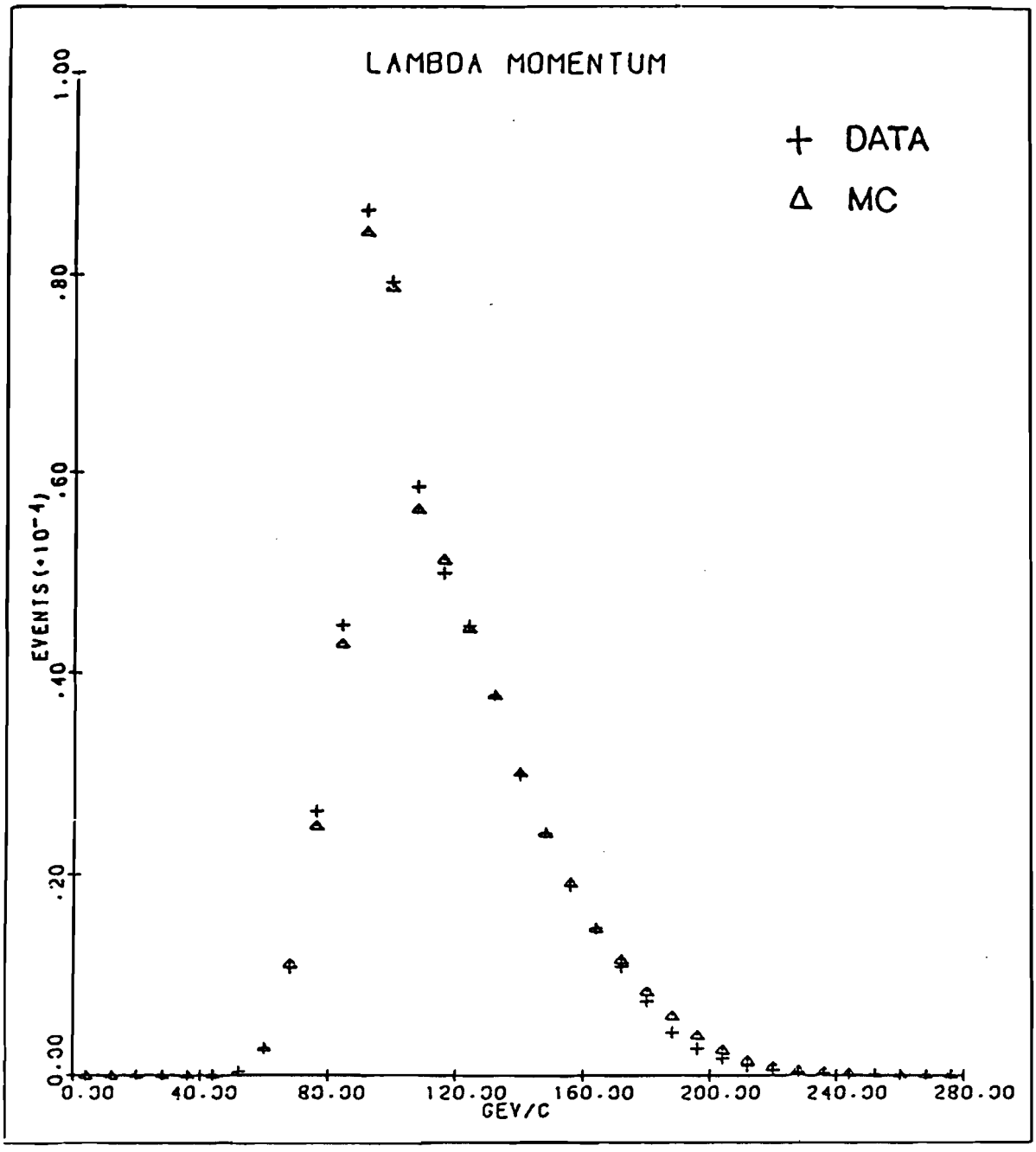

Figure 31. Lambda Momentum - Lambda Beta Decays

The lambda decay vertex distribution is shown for the fiducial region between the ends of the evacuated pipe, chosen to remove events originating from neutral beam interactions in any window material.

The ratio of the difference between the two solutions for the lambda momentum to their sum is shown in Figure 29 for the unadjusted events. The D_o^2 distribution for the adjusted events is presented in the following plot.

The construction of a distribution for a variable defined in the lambda rest frame required a procedure for handling the lambda momentum ambiguity. One choice was to use the more probable solution with a value closest to the peak at 95 GeV/c of the lambda momentum spectrum corresponding to the final lambda beta decay sample. This was determined with the Monte Carlo, which indicated that such a procedure chose the correct solution 80% of the time. A distribution in the lambda rest frame thus consisted of the preferred solutions from the unadjusted events, as well as the unambiguous solutions from the adjusted events. The lambda momentum distribution of the final lambda beta decay sample, constructed according to this procedure, is compared to the corresponding Monte Carlo simulation in Figure 31.

5.2 The Axial Vector to Vector Coupling Constant Ratio

The determination of g_A/g_V was accomplished by measuring the angular distribution of the neutrino relative to the electron direction in the lambda rest frame. A value for the cosine of the angle between the electron and the neutrino directions, denoted x, was calculated for each event. The experimental x distribution, which was sensitive to the magnitude of the coupling constant ratio, was then compared to the corresponding distribution from the Monte Carlo simulation. The value of g_A/g_V, denoted y, was varied in the differential decay rate F(e,x;y) used to generate the lambda beta decays in the Monte Carlo simulation.

5.2.1 The Differential Decay Rate

The function representing the differential decay rate for lambda beta decay can be written:

$$\frac{d^2\Gamma}{de\,dx} \propto F(e,x;y) = \frac{\beta e^2 (e_m - e)^2}{\left[1 - \frac{e}{M_A}(1-\beta x)\right]^3}\left[D_1(e,x;y) + x\beta D_2(e,x;y)\right]$$

This Dalitz plot density is characterized by the value of

g_A/g_V , denoted y, and by the two variables e and x. Each of the functions D_1 and D_2 can be expressed in terms of three different functions of y [13]:

$$D_1(e,x:y) = A(y) + (e/M_\Lambda)\, C(y) + (\sqrt{}/M_\Lambda)\, E'(y)$$

$$D_2(e,x:y) = B(y) + (e/M_\Lambda)\, D(y) + (\sqrt{}/M_\Lambda)\, F(y).$$

The six functions of y are

$$A(y) = t + (2-r)s^2 + (2+r)y^2$$
$$B(y) = t + rs^2 - ry^2$$
$$C(y) = -s^2 - 2w^2 - y^2 - 2sy$$
$$D(y) = +s^2 - 2w^2 + y^2 + 2sy$$
$$E'(y) = -s^2 - 2w^2 - y^2 + 2sy$$
$$F(y) = +s^2 - 2w^2 + y^2 - 2sy.$$

The constants s and t are defined by

$$s = 1 + (1+r)w$$
$$t = (1+r)2w(w-s).$$

The constant r is the ratio of the proton mass to the lambda mass. The constant w is the ratio of the weak magnetism coupling constant g_W to the vector coupling constant g_V , which can be predicted by applying the

conserved vector current hypothesis and SU(3) symmetry arguments to the members of the baryon octet [6]. This will be discussed further in the final chapter.

5.2.2 The Measurement

A least squares technique was used to minimize:

$$\chi^2(y) = \sum_{i=1}^{20} \frac{\left(R_i - \frac{M_i(y)}{N(y)}\right)^2}{R_i + \frac{M_i(y)}{(N(y))^2}}$$

The sum was performed over the twenty bins in the x distribution. R_i was the population of bin i for the experimental distribution. $M_i(y)$ represented the population of bin i in the distribution corresponding to a Monte Carlo event sample generated with a given value of y. The overall normalization for such a Monte Carlo distribution was $N(y) = (\sum_i M_i(y))/(\sum_i R_i)$, typically a factor of five to seven. The value of χ^2 is plotted as a function of y in Figure 32.

The two minima of the function $\chi^2(y)$ illustrate the sensitivity of the x distribution to the magnitude of y.

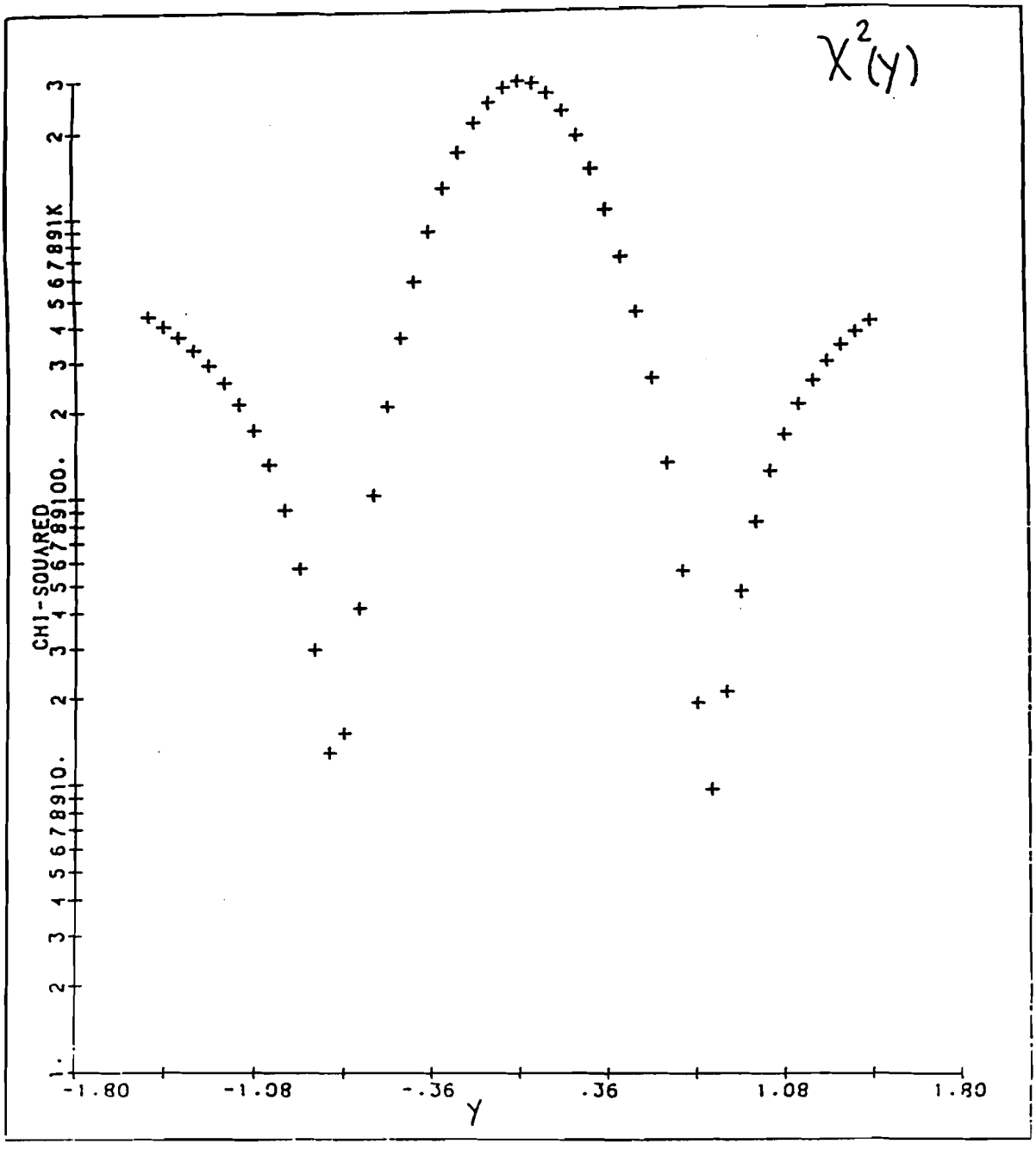

Figure 32. $\chi^2(y)$ for the x Distribution

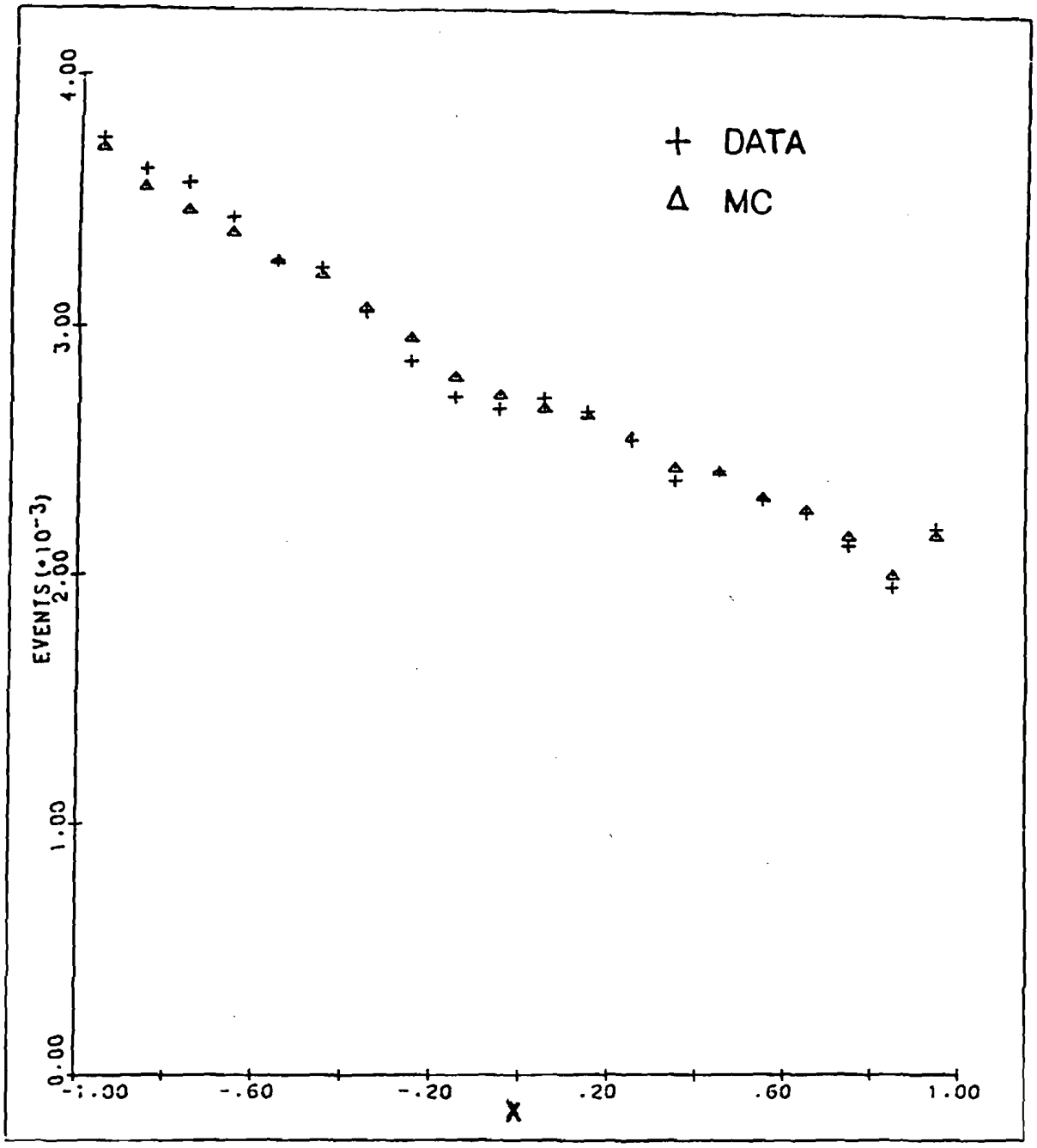

Figure 33. x Distribution Comparison with Monte Carlo (y_+)

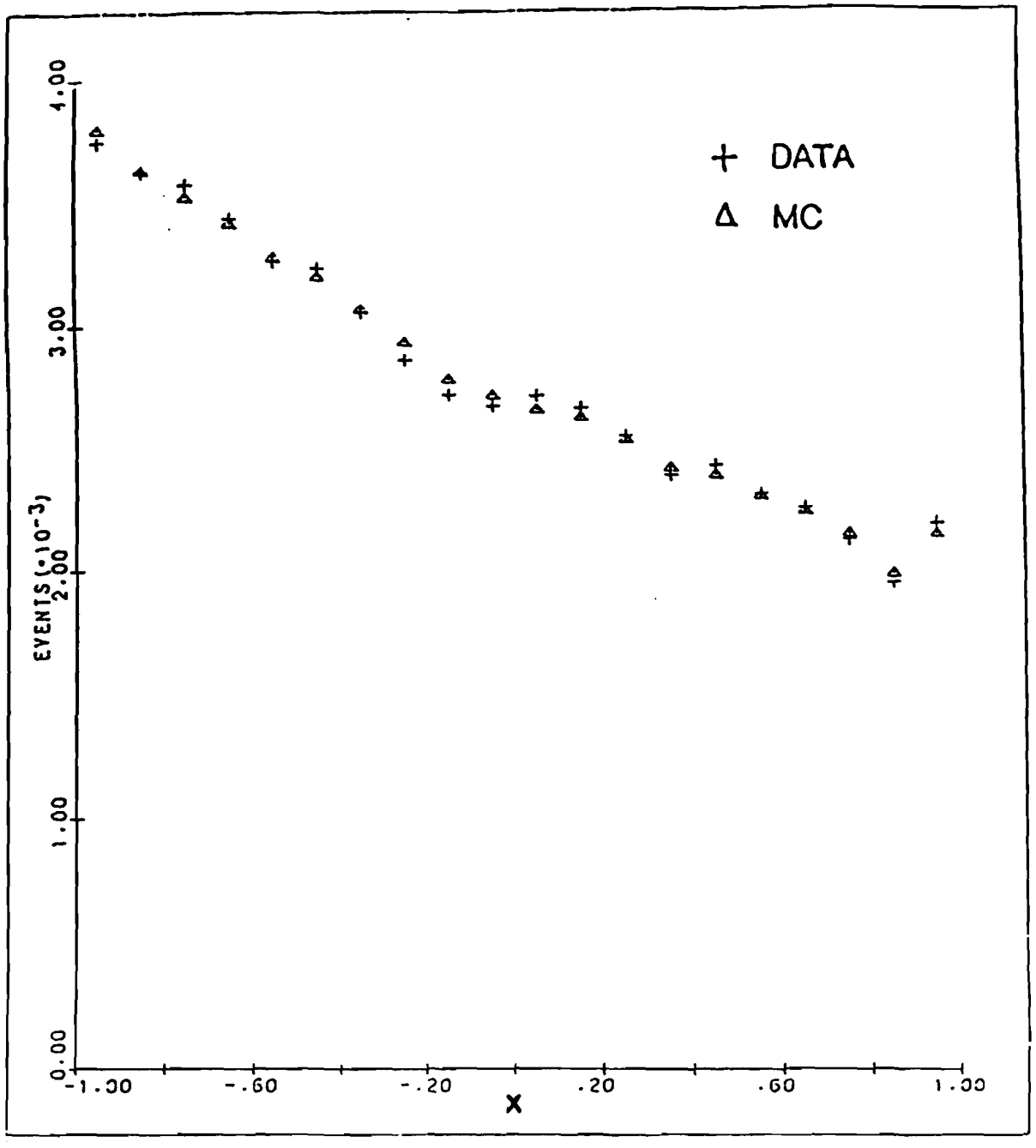

Figure 34. x Distribution Comparison with Monte Carlo (y_-)

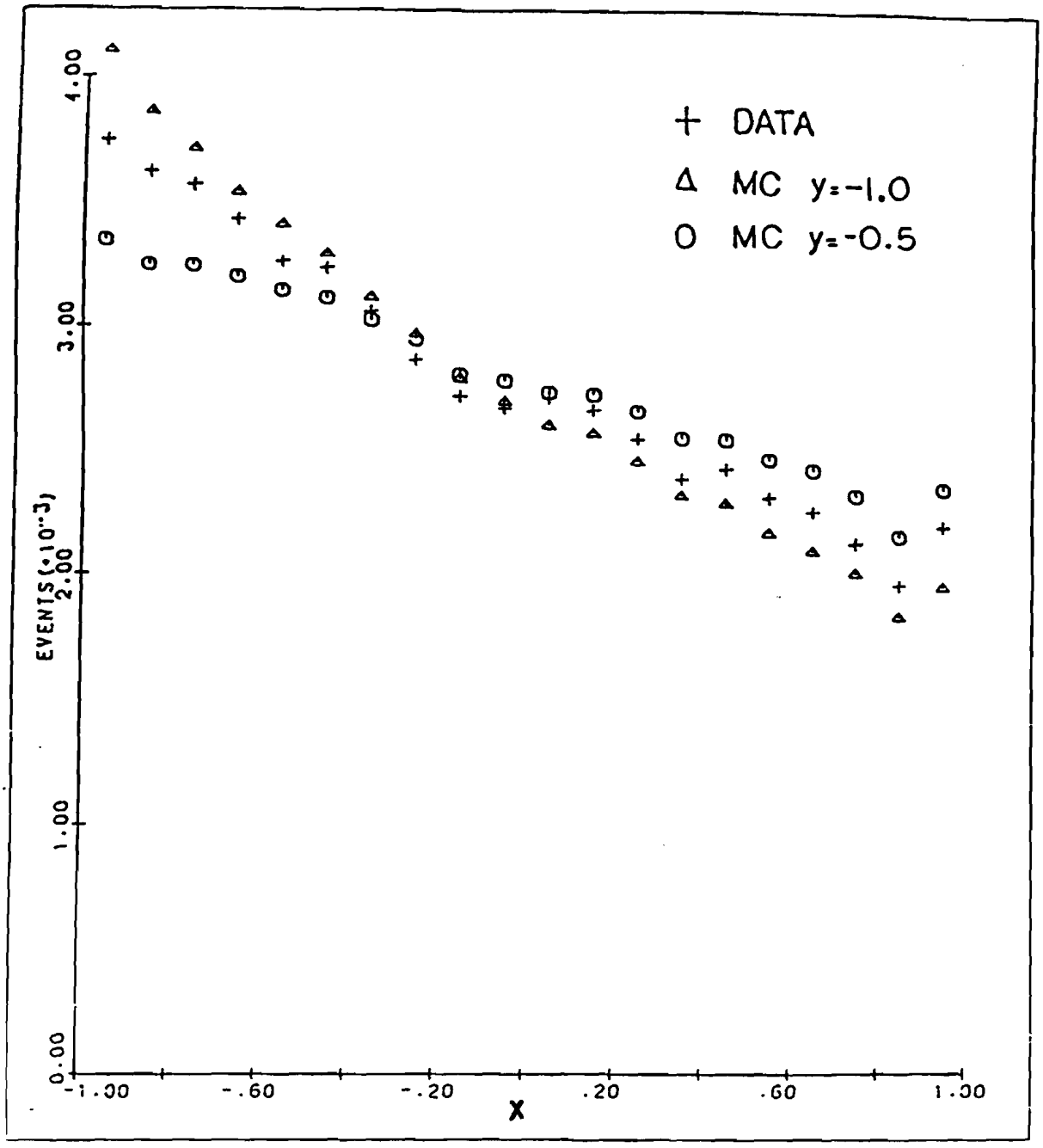

Figure 35. x Distribution Comparison with Other y Values

The minima are located at:

$$y_- = -0.757 \pm 0.019 \quad (\chi^2/df = 11.5/19)$$

and

$$y_+ = +0.777 \pm 0.019 \quad (\chi^2/df = 9.7/19) \ .$$

The error is purely statistical, reflecting the change in y corresponding to an increase of one unit over the value of $\chi^2(y)$ at the minimum. Comparisons of the x distribution of the experimental data with the Monte Carlo distributions corrresponding to the values $y=y_+$ and $y=y_-$ are presented in Figures 33 and 34. The Monte Carlo distributions for two other values of y are compared to the experimental distribution in the following plot.

The systematic error presently assigned to the result for g_A/g_V is ± 0.080, equivalent to 10% of the result itself. At the moment, the result for g_A/g_V depends on the procedure used to handle the lambda momentum ambiguity for the unadjusted events. The same procedure is applied to both the experimental data and the Monte Carlo simulation in order to form their respective x distributions for a subsequent comparison; the procedure used to obtain the results presented in Figure 32 has been described on page 102. The quoted shift results when this procedure is modified so that the solution chosen to

contribute to the x distribution for both the experimental data and the Monte Carlo simulation is the one with its lambda momentum closest to the mean value at 112 GeV/c of the lambda momentum spectrum. Work is in progress to improve the Monte Carlo simulation so that the result for g_A/g_V is independent of this procedure.

5.3 The Branching Ratio

The calculation of the branching ratio for lambda beta decay proceeds according to:

$$\frac{\Gamma(\Lambda \to p e^- \bar{\nu}_e)}{\Gamma(\Lambda \to all)} = \frac{N_\beta \, p \, b_\pi}{512 \, N_\pi \, \epsilon_A \epsilon_e \epsilon_p \epsilon_s} \quad ,$$

where

- N_β is the number of lambda beta decays in the final semi-leptonic sample (N_β =55,752),

- p is the purity of the lambda beta decay sample, accounting for the Ke3 and residual non-leptonic lambda decay background ($p=0.97\pm0.01$),

- $512\ N_{\pi}$ is the product of the prescaling factor for the V trigger and the number of non-leptonic lambda decays in the final prescaled sample (N_{π} =422,453),

- b_{π} is the branching ratio for $\Lambda \rightarrow p\pi^-$:

$$\frac{\Gamma(\Lambda \rightarrow p\pi^-)}{\Gamma(\Lambda \rightarrow all)} = 0.642 \pm 0.005 ,$$

- ϵ_A is the product of the geometrical acceptance, the V trigger efficiency, the reconstruction efficiency and the offline fiducial cuts for the lambda beta decay mode relative to the non-leptonic $\Lambda \rightarrow p\pi^-$ decay mode, integrated over the lambda momentum spectrum ($\epsilon_A = 0.41 \pm 0.02$),

- ϵ_e is the product of the online and offline efficiencies of the electron signatures required by the lead glass and synchrotron radiation detectors for the integrated spectrum of the lambda beta decay electrons entering the detectors ($\epsilon_e = 0.68 \pm 0.04$),

- ϵ_p is the proton detection efficiency of the threshold Cerenkov counter for the integrated spectrum of lambda beta decay protons entering

the counter ($\epsilon_p = 0.93 \pm 0.02$),

and

- ϵ_s is the semi-leptonic selection efficiency. This accounts for the effects of the D_o^2 requirement on the adjusted events, and for the loss of lambda beta decays as a result of the invariant mass requirements ($\epsilon_s = 0.76 \pm 0.02$).

The systematic errors, which dominate the result, have been included in the quoted efficiencies.

The evaluation of the expression for the branching ratio yields the value $(8.15 \pm 0.69) \times 10^{-4}$.

5.4 Results

This experiment has determined the ratio of the axial vector to vector coupling constants in lambda beta decay. There are two results, with opposite signs:

$$g_A/g_V = -0.757 \pm 0.019 \pm 0.080$$
$$g_A/g_V = +0.777 \pm 0.019 \pm 0.080 \quad .$$

The experiment has also determined the branching ratio for lambda beta decay:

$$\frac{\Gamma(\Lambda \to p e^- \bar{\nu}_e)}{\Gamma(\Lambda \to all)} = (8.15 \pm 0.69) \times 10^{-4} ,$$

where the systematic errors have been included in the result.

The accuracy of these results will improve as the systematic effects become better understood through work which is presently in progress.

CHAPTER 6

DISCUSSION

6.1 Theoretical Predictions

The Cabibbo theory predicts relationships between the hyperon semi-leptonic decay processes. The assumptions of the model are: (1) that the interaction is V-A and the weak vector current belongs to the same SU(3) octet as the electromagnetic current; (2) that the axial vector currents are the same components of another SU(3) octet; and (3) that the leptonic current is coupled to a single hadronic current of unit length ($J_\mu^h = \cos\theta_c\, J_\mu^{\Delta S=0} + \sin\theta_c\, J_\mu^{\Delta S=1}$). The extension to strangeness changing currents of the Conserved Vector Curent hypothesis, which postulates that the charged vector

currents coupled to leptons are conserved isospin currents, is accomplished by (1); the weak magnetism coupling constants for the hyperon semi-leptonic decays can thus be related to the anomolous magnetic moments of the neutron and proton. The axial vector currents are related by (2); the axial vector coupling constant (g_A) can be calculated in terms of θ_c and the values of the antisymmetric and symmetric SU(3) reduced matrix elements F and D. The Cabibbo angle θ_c, introduced in (3), accounts for the suppression of $\Delta S=1$ decays. An excellent review is provided by Jarlskog [14].

The predictions of the Cabibbo model for lambda beta decay are [6]:

$$g_A = (3/2)^{1/2} \sin\theta_c \, (F+D/3)$$

$$g_V = - (3/2)^{1/2} \sin\theta_c$$

$$g_W = - (3/2)^{1/2} \sin\theta_c \, \frac{M_\Lambda \mu_p}{2M_p} \quad .$$

A recent fit [6] to the three parameters in the theory ($F, D, \sin\theta_c$) using the available experimental hyperon semi-leptonic data yields

$$F = 0.437 \qquad D = 0.832 \qquad \sin\theta_c = 0.223 \quad .$$

This corresponds to a value for g_A/g_V of -0.715 and a branching ratio of 8.34×10^{-4}.

Various quark model calculations also predict values for g_A/g_V [15]. The SU(6) non-relativistic quark model, in which the baryons are composed of three spin-1/2 quarks, predicts a value of -1.0 for lambda beta decay. This can be modified by incorporating refinements in the calculations, such as different quark masses, hyperfine interactions between quarks and relativistic effects. One estimate of these corrections depresses the simple prediction to -0.79 [16].

6.2 Other Experimental Results

A summary of experimental results on lambda beta decay is given in Table 1. A reference, the year of publication, the number of events used to determine the axial vector to vector coupling constant ratio, the branching ratio measurement, and finally, the coupling constant ratio, are presented for each experiment.

The experimental distribution used to determine the coupling constant ratio is noted by the letter appearing next to the result. Results obtained from polarized lambda

hyperons are derived from an analysis of the correlations between the spin direction of the decaying lambda and the direction of a decay product in the lambda rest frame. These spin asymmetry distributions are sensitive to both the magnitude and sign of g_A/g_V. The experiments performing such an analysis agree that the sign is negative. The magnitude obtained from the spin asymmetry distributions can be seen to be consistently lower than the results obtained by examining the electron-neutrino correlation, the decay baryon spectrum or the entire Dalitz plot.

The final data sample presented here is unpolarized; it can be divided into polarized subsamples, each with an average polarization of 8%. These subsamples correspond to different signs of the production angle. Previous data published by the Neutral Hyperon Collaboration at Fermilab has been divided in such a manner [17]. This thesis does not discuss the spin asymmetry distributions. The analysis of these distributions will be the subject of future work.

The presence or absence of two corrections in the experimental analysis of the data from which each of the results listed in Table 1 were obtained is explicitly noted. These corrections are discussed in detail by Garcia [6]. The analysis of the data in this thesis did not

incorporate these corrections. The first accounts for radiative corrections to the hyperon semi-leptonic process. The second concerns the fact that the coupling constants g_A and g_V defined for the hadronic matrix element in Chapter 1 are actually the values of the leading weak form factors evaluated at a value of zero for the square of the four-momentum transfer , that is, $g_V = f(q^2 = 0)$ and $g_A = g(q^2 = 0)$. It has been traditional to neglect the q^2 dependence of the leading weak interaction form factors because of the low value for the maximum q^2 attained in lambda beta decay (0.03 GeV^2), although some experiments have chosen to include form factors which are linear functions of q^2 .

Both corrections become more important for experiments with high statistics which attempt to obtain precise measurements of the coupling constants. The value for $|g_A/g_V|$ obtained from the recent high statistics Brookhaven - U. Mass. experiment (described in reference 19) was 0.734 ± 0.031; it included a prescription for incorporating these corrections. They reported that the result increased by 0.1 when these corrections were neglected, with the q^2 dependence accounting for 10% of the shift. The value of $|g_A/g_V|$ presented in the unpublished thesis of J. Wise [27] , which did not account for either correction in the analysis of the data, was

0.90 ± 0.17 . The preliminary results from the recent CERN SPS experiment, described in reference 18, are also presented in Table 1. This experiment confirms that the sign of g_A/g_V is negative. A value of 0.748 ± 0.037 for $|g_A/g_V|$ was obtained when q^2 and radiative corrections were neglected in the analysis of the 7000 events comprising the final data sample. The value shifted to 0.699 ± 0.035 when a q^2 dependence for the form factors was included. The final radiative corrections to be incorporated into the analysis are presently being calculated by three Hungarian theorists; Toth, Margaritisz and Szego [28].

6.3 Conclusion

The results from this experiment are, in general, consistent with the results from the other lambda beta decay experiments. They all support the conclusion that the Cabibbo theory and quark models can make predictions valid up to 20%. An analysis incorporating radiative corrections and a q^2 dependence for the leading weak interaction form factors is necessary before a precision measurement can be compared to theoretical models. A precise measurement of g_A/g_V would provide clearer experimental guidance in determining the refinements in

quark model calculations necessary to bring theoretical predictions into better agreement with experimental results, as well as distinguishing among models incorporating symmetry breaking into the Cabibbo SU(3) framework [29].

APPENDIX

TABLE 1. Experimental Results for Lambda Beta Decay

Reference (Year)	No. events	Branching Ratio ($\times 10^4$)	$\lvert g_A/g_V \rvert$
This Expt.	55752	8.15±0.69	$\left\{\begin{matrix}-0.757\pm0.019\pm0.080\\ +0.777\mp0.019\mp0.080\end{matrix}\right\}$ c
18 (1981) f	7000	8.33±0.35	0.748±0.037 c 0.699∓0.035 a,c
19 (1981)	10037	8.43±0.17	0.734±0.031 a,b,c,e
20 (1977)	441	7.9±0.7	0.53(-0.09)(+0.11) e 0.68(-0.11)(+0.14) a,b,c 0.60(-0.10)(+0.13) c 0.33(-0.09)(+0.14) d
21 (1976)	405		0.47±0.10 e 0.52∓0.09 a,c 0.40∓0.09 a,d
22 (1973)	817	8.4±0.4	0.63±0.06 e 0.64∓0.06 c 0.33(-0.11)(+0.20) d
23 (1972)	352		0.74(-0.09)(+0.12) c,e
24 (1971)	141	7.8±0.9	0.75(-0.15)(+0.18) c,e
25 (1969)	204	8.0±0.8	0.72(-0.14)(+0.19) c,e
26 (1965)	Review		1.14(-0.23)(+0.33) e

a. q^2 correction included
b. radiative corrections included
c. electron neutrino correlation/c.m. proton spectrum/Dalitz plot analysis
d. spin asymmetry distribution analysis
e. Particle Data Group listing
f. Preliminary Values

REFERENCES

REFERENCES

1. See, for example, R.E. Marshak, Riazuddin, and C.P. Ryan, "Theory of Weak Interactions in Particle Physics", (Wiley, New York,1969)

2. Particle Data Group, Review of Particle Properties, Phys. Lett. 111B, 1 (1982)

3. A. Garcia, Phys. Rev. D25, 1348 (1982)

4. A. Garcia, Phys. Rev. D3, 2638 (1971)

5. N. Cabibbo, Phys. Rev. Lett. 10, 531 (1963)

6. A. Garcia and P. Kielanowski, Phys. Rev. D26, 1090 (1982)

7. P, Skubic et. al., Phys. Rev. D18, 3115 (1978)

8. R. Grobel, Ph.D. thesis, "The Measurement of Lambda, K-Short, and Lambda Bar Production and Lambda Polarization from Interactions of 400 GeV/c Protons with Hydrogen", (University of Wisconsin, 1980, unpublished)

9. P. Skubic, Ph.D. thesis, "Neutral Strange Particle Production from Nuclear Targets by 300 GeV Protons", (University of Michigan, 1977, unpublished)

10. W.H. Tucker, "Radiation Processes in Astrophysics", (MIT Press, Cambridge, Massachusetts, 1975)

11. F. Sauli, "Principles of Operation of Multiwire Proportional and Drift Chambers", CERN Report 77-0 (1 77)

12. J.E. Bateman, M.W. Waters, and R.E. Jones, Nuc. Instr. Meth. 135, 235 (1976)

13. A. Garcia and P. Kielanowski, "Some Theorems on the Determination of Form Factors in Unpolarized Hyperon Semi-Leptonic Decay", preprint, to appear in Phys. Lett. 191B (1983)

14. C. Jarlskog, "Phenomenology of Weak Interactions", CERN Report 74-22 (1974)

15. C. Quigg, "Models for Hadrons",
Fermilab Report Conf.81/75-THY (1981)

16. P. Bracken, A. Frenkel, and G. Karl,
Phys. Rev. D24, 2948 (1981)

17. K. Heller et. al., Phys. Rev. Lett. 41, 607 (1978)

18. D. Froidevaux, Ph.D. thesis, "Disintegrations
Semi-Leptoniquess d´Hyperons",
(L´Universite de Paris-Sud, 1981, unpublished)

19. J. Wise et al.., Phys. Lett. 98B, 123 (1981)

20. J. Lindquist et. al., Phys. Rev. D16, 2104 (1977)

21. T.H. Burnett et. al., Nuovo Cimento 34, 14 (1976)

22. K.H. Althoff et. al., Phys. Lett. 43B, 237 (1973)

23. N. Baggett et. al., Z. Phys. 249, 279 (1972)

24. J. Canter et. al., Phys. Rev. Lett. 26, 868 (1971)

25. M. Maloney et. al., Phys. Rev. Lett. 23, 425 (1969)

26. G. Conforto, Review - Herzegnovi Conference (1965)

27. J. Wise, Ph.D. thesis,"A High Statistics Measurement
of the Vector and Axial Vector Coupling Constants in
Lambda Beta Decay", (University of Massachusetts,
1979, unpublished)

28. K. Toth, T. Margaritisz, and K.S Szego,
Preprint, Th.3169 CERN (1981)

29. A. Garcia and P. Kielanowski, "Symmetry Breaking and
Higher Representations in the Cabibbo Theory",
preprint, to appear in Phys. Rev. D (1982)